

# **Photophysics of Poly(3-hexylthiophene):Non-Fullerene Acceptor Organic Solar Cells**

Thesis by  
Wejdan Althobaiti

In Partial Fulfillment of the Requirements  
For the Degree of  
Master of Science

King Abdullah University of Science and Technology  
Thuwal, Kingdom of Saudi Arabia

July, 2021

## **EXAMINATION COMMITTEE PAGE**

The thesis of Wejdan Althobaiti is approved by the examination committee.

Committee Chairperson: Dr. Frédéric Laquai

Committee Members: Dr. Iain McCulloch, Dr. Thomas Anthopoulos

© July, 2021

Wejdan Althobaiti

All Rights Reserved

## ABSTRACT

### **Photophysics of Poly(3-hexylthiophene):Non-Fullerene Acceptor Organic Solar Cells**

Wejdan Althobaiti

Insight into the relationship between the Ionization Energy (IE) offsets between donor and acceptor materials and the performance of the organic solar cells (OSC) could improve the charge generation efficiency. Charge generation can proceed through two different paths in Bulk Heterojunction (BHJ) based OSCs which are electron transfer from donor to acceptor and hole transfer from acceptor to donor. Electron transfer can be controlled by electron affinities and hole transfer can be controlled by ionization energies. In this work, large IE offsets were investigated in poly(3-hexylthiophene-2,5-diyl)(P3HT):Non Fullerene Acceptor (NFA) based OSCs by fabricating and characterizing devices, also conducting several experiments to optimize the processing conditions for the devices. These results provide an overview of the charge transfer and IE offsets dependence, also a general picture of the photophysics in P3HT:NFAs based OSCs. Moreover, using wide bandgap polymer donor which has shallow IE such as P3HT with low-bandgap NFAs may provide sufficient IE offsets between donor and acceptors enabled us to reach the inverted Marcus regime. In this regime, the electron transfer rate decreases upon decreasing the charge transfer (CT) state energy compared to the exciton energy. The decrease of the internal quantum efficiency (IQE) upon increasing the IE offset suggests that we are in that regime.

## ACKNOWLEDGEMENTS

All praise and thanks are due to the almighty Allah, who granted me the determination and strength to complete this work.

First, I would like to express my sincere gratitude and appreciation to my advisor Dr. Frédéric Laquai for his continuous support, generous guidance and patience

Special thanks to Dr. Julien Gorenflot and Dr. Jafar Khan for putting their valuable time into this thesis. I appreciate it more than I can say.

I would like to extend my thanks to my colleagues and friends of Ultrafast Dynamics Group, for their help and support.

To my KAUSTIAN friends at H-4301, thank you for your help and guidance as this journey would not have been possible without your support.

To my beautiful family, there are no words that can describe how much I appreciate everything you have done and you are still doing for me. Thanks a lot.

## TABLE OF CONTENTS

<b>EXAMINATION COMMITTEE PAGE</b> .....	<b>2</b>
<b>COPYRIGHTS</b> .....	Error! Bookmark not defined.
<b>ABSTRACT</b> .....	<b>4</b>
<b>ACKNOWLEDGEMENTS</b> .....	<b>5</b>
<b>TABLE OF CONTENTS</b> .....	<b>6</b>
<b>LIST OF ABBREVIATIONS</b> .....	<b>9</b>
<b>LIST OF CHEMICAL MOLECULES</b> .....	<b>11</b>
<b>LIST OF SYMBOLS</b> .....	<b>12</b>
<b>LIST OF ILLUSTRATIONS</b> .....	<b>13</b>
<b>LIST OF TABLES</b> .....	<b>15</b>
<b>Chapter 1: Introduction</b> .....	<b>16</b>
<b>Chapter 2: Theoretical Background</b> .....	<b>20</b>
2.1 Solar radiation and photovoltaic effect / efficiency .....	20
2.2 Organic Solar Cells (OSCs) .....	21
2.2.1 Organic Semiconductors .....	22
2.2.2 Structures of organic photovoltaic devices .....	25
2.3 Working mechanism of organic photovoltaics.....	27
2.3.1 Photon absorption and exciton generation .....	27
2.3.2 Exciton diffusion .....	28
2.3.3 Exciton dissociation and charge separation .....	28
2.3.4 Charge transport and extraction .....	29
2.4 Characterization of organic solar cells .....	29
2.4.1 Current-Voltage Characterization .....	29
2.4.2 External quantum efficiency (EQE).....	31
2.4.3 Internal quantum efficiency (IQE).....	32
2.5 Preparation of organic solar cells .....	33
2.5.1 Photoactive materials .....	33

2.5.2 Solvents .....	34
2.5.3 Coating techniques .....	34
2.6 Energy levels and their determination.....	35
2.6.1 Electron affinity and ionization energy .....	35
2.6.2 Role of ionization energy level offsets.....	38
2.6.3 Marcus Theory .....	43
2.7 P3HT-based organic solar cells.....	48
2.7.1 P3HT .....	48
2.7.2 P3HT:Fullerene acceptors .....	48
2.7.3 P3HT:Non-Fullerene acceptors.....	49
<b>Chapter 3: Materials and Methods .....</b>	<b>51</b>
3.1 Investigated materials.....	51
3.1.1 Donor and acceptor materials.....	51
3.1.2 Device preparation and optimization .....	55
3.1.3 Device Layers.....	61
3.1.3.1 Substrates cleaning process.....	61
3.1.3.2 Electron collecting electrode.....	61
3.1.3.3 Electron transporting layer .....	62
3.1.3.4 Active layer .....	62
3.1.3.5 Hole transporting layer.....	63
3.1.3.6 Hole collecting layer .....	63
3.2 Device Characterization Techniques.....	64
3.2.1 J-V Characterization.....	64
3.2.2 External Quantum Efficiency (EQE) .....	64
3.3 UV-Vis Spectrophotometry.....	64
3.4 Photoluminescence Spectroscopy .....	65
3.5 Profilometer.....	65
<b>Chapter 4: Results and Discussion .....</b>	<b>66</b>
4.1 UV-vis Absorption and Photoluminescence (PL) / Optical bandgaps .....	66
4.2 J-V Characteristics .....	70
4.3 External Quantum Efficiency (EQE) .....	73
4.3 Internal Quantum Efficiency (IQE).....	74

<b>Chapter 5: Conclusion and Future Work.....</b>	<b>79</b>
5.1 Conclusion.....	79
5.2 Future work .....	80
5.2.1 Exciton Quenching / Charge Transfer.....	80
5.2.2 Charge Recombination.....	80
5.2.3 Morphology Studies .....	80
<b>BIBLIOGRAPHY .....</b>	<b>81</b>

**LIST OF ABBREVIATIONS**

A	Acceptor
BHJ	Bulk heterojunction
CB	Chlorobenzene
CF	Chloroform
CF	Chloroform
CN	Chloronaphthalene
CT	Charge transfer
D	Donor
DIO	1,8diodooctan
EA	Electron Affinity
EQE	External quantum efficiency
FF	Fill factor
HOMO	Highest occupied molecular orbital
IE	Ionization Energy
IQE	Internal quantum efficiency
J <sub>sc</sub>	Short-circuit current
J-V	Current density-voltage
LUMO	Lowest occupied molecular orbital
NFA	Non-fullerene acceptor
NIR	Near-infrared
OPVs	Organic photovoltaics
OSCs	Organic solar cells
PCE	Power conversion efficiency
PL	Photoluminescent

PN	1-phenylnaphthalene
PVs	Photovoltaics
Si	Silicon
TR-PL	Time-Resolved Photoluminescence
UV	Ultraviolet
UV-Vis	Linear optical absorption spectroscopy in the Ultraviolet and Visible spectral Region.
VdW	Van-der-Waals
VIS	Visible
V <sub>oc</sub>	Open-circuit voltage

## LIST OF CHEMICAL MOLECULES

Polymer/Molecule	International Union of Pure and Applied Chemistry (IUPAC)
P3HT	poly(3-hexylthiophene-2,5-diyl)
BT-CIC	2-[(2Z)-5,6-dichloro-2-[[20-[(Z)-[5,6-dichloro-1-(dicyanomethylidene)-3-oxoinden-2-ylidene]methyl]-2,14-bis(2-ethylhexoxy)-5,5,17,17-tetrakis(4-hexylphenyl)-9,12,21,24-tetrathiaheptacyclo[13.9.0.0 <sup>3,13</sup> .0 <sup>4,11</sup> .0 <sup>6,10</sup> .0 <sup>16,23</sup> .0 <sup>18,22</sup> ]tetracos-1(15),2,4(11),6(10),7,13,16(23),18(22),19-nonaen-8-yl]methylidene]-3-oxoinden-1-ylidene]propanedinitrile
IT-4F	2-[(2Z)-2-[[20-[(Z)-[1-(dicyanomethylidene)-5,6-difluoro-3-oxoinden-2-ylidene]methyl]-12,12,24,24-tetrakis(4-hexylphenyl)-5,9,17,21-tetrathiaheptacyclo[13.9.0.0 <sup>3,13</sup> .0 <sup>4,11</sup> .0 <sup>6,10</sup> .0 <sup>16,23</sup> .0 <sup>18,22</sup> ]tetracos-1(15),2,4(11),6(10),7,13,16(23),18(22),19-nonaen-8-yl]methylidene]-5,6-difluoro-3-oxoinden-1-ylidene]propanedinitrile
IEICO	2,2'-[[[4,4,9,9-Tetrakis(4-hexylphenyl)-4,9-dihydro-s-indaceno[1,2-b:5,6-b']dithiophene-2,7-diyl]bis]] [[4-[(2-ethylhexyl)oxy]-5,2-thiophenediyl]methylidyne(5,6-difluoro-3-oxo-1H-indene-2,1(3H)-diylidene)]bis[propanedinitrile]
IEICO-4F	2,2'-[[[4,4,9,9-Tetrakis(4-hexylphenyl)-4,9-dihydro-s-indaceno[1,2-b:5,6-b']dithiophene-2,7-diyl]bis]] [[4-[(2-ethylhexyl)oxy]-5,2-thiophenediyl]methylidyne(5,6-difluoro-3-oxo-1H-indene-2,1(3H)-diylidene)]bis[propanedinitrile]
IEICO-4Cl	2,2'-((2Z,2'Z)-(((4,4,9-tris(4-hexylphenyl)-9-(4-pentylphenyl)-4,9-dihydro-s-indaceno[1,2-b:5,6-b]dithiophene-2,7-diyl)bis(4-((2-ethylhexyl)oxy)thiophene-5,2-diyl bis(methanylylidene))bis(5,6-dichloro-3-oxo-2,3-dihydro-1H-indene)))dimalononitrile
O-IDTBR	(5Z,5'Z)-5,5'-((7,7'-(4,4,9,9-tetraoctyl-4,9-dihydro-s-indaceno[1,2-b:5,6-b']dithiophene-2,7-diyl)bis(benzo[c][1,2,5]thiadiazole-7,4-diyl))bis(methanylylidene))bis(3-ethyl-2-thioxothiazolidin-4-one)

**LIST OF SYMBOLS**

$L_D$	Exciton diffusion length
$k_{ET}$	Electron transfer rate
$c$	Speed of light ( $2.99792 \times 10^8 m/s$ )
$h$	Planck's constant ( $6.626 \times 10^{-34} J.s$ )
$\lambda$	Photon wavelength
$\pi$	Pi bonds
$\sigma$	Sigma bonds
$\tau$	Lifetime
$k(\lambda)$	Extinction coefficient
$n(\lambda_i)$	Refractive index
$\Delta G^\ddagger$	Driving force
$\alpha(\lambda)$	Absorption coefficient

## LIST OF ILLUSTRATIONS

<b>Figure 1:</b> Renewable and total energy consumption (2019). <sup>[4]</sup> .....	16
<b>Figure 2:</b> Growth of efficiencies for a range of photovoltaic technologies. <sup>[7]</sup> .....	18
<b>Figure 3:</b> Solar radiation spectrum. <sup>[10]</sup> .....	20
Figure 4: Molecular structure of conjugated polymers and small molecules. <sup>[12]</sup> .....	21
<b>Figure 5:</b> sp, sp <sup>2</sup> , and sp <sup>3</sup> hybrid orbitals. <sup>[15]</sup> .....	23
<b>Figure 6:</b> HOMO and LUMO formation. <sup>[16]</sup> .....	24
<b>Figure 7:</b> Energy bands diagram of Inorganic and Organic semiconductors. ....	25
<b>Figure 8:</b> Different device structures a) single layer b) bilayer and c) bulk heterojunction(BHJ). <sup>[18]</sup> .....	26
<b>Figure 9:</b> OPVs working mechanism. <sup>[20]</sup> .....	27
<b>Figure 10:</b> Schematic of J-V curve (black line) and power voltage (red line) of a solar cell under illumination. <sup>[23]</sup> .....	30
<b>Figure 11:</b> Comparison between ideal and experimental EQE spectra for Si solar cell <sup>[25]</sup> .....	31
<b>Figure 12:</b> IQE, EQE, and reflectance spectra. <sup>[24]</sup> .....	32
<b>Figure 13:</b> Chemical structures of donor and acceptor materials in OPVs. <sup>[22]</sup> .....	33
<b>Figure 14:</b> Spin coating processes. <sup>[28]</sup> .....	35
<b>Figure 15:</b> Energy levels diagram, $W_A$ is the work function of the anode, $W_C$ is the work function of the cathode in open circuit conditions. <sup>[29]</sup> .....	36
<b>Figure 16:</b> Semiconductor heterojunction energy band diagram. <sup>[29]</sup> .....	37
<b>Figure 17:</b> Energy levels schematic shows electron and hole transfer. $\Delta IE$ is the IE offset, and $\Delta EA$ is EA offset. <sup>[21]</sup> .....	38
<b>Figure 18:</b> Energy levels of different materials. b) Relation between IE offsets and averaged IQE, symbols are for D:A system, D indicated in the legend and A written next to the symbol. <sup>[30]</sup> .....	39
<b>Figure 19:</b> Band bending at the interface between donor and acceptor. <sup>[30]</sup> .....	40
<b>Figure 20:</b> a) Relation between PLQ and IQE vs. IE offsets b) Band bending (B) for large IE offsets. <sup>[30]</sup> .....	41
<b>Figure 21:</b> a) relation between PLQ and IQE against IE offsets b) band bending (B) with large IE offsets. <sup>[30]</sup> .....	42
<b>Figure 22:</b> Potential energy surfaces of donor and acceptor. <sup>[23][34]</sup> .....	44
<b>Figure 23:</b> Potential energy surfaces of excited ( $D^* A$ ) and charge transfer ( $D^+ A^-$ ) states represented by parabolas. <sup>[23]</sup> .....	45
<b>Figure 24:</b> Marcus Theory Diagram indicating the normal and inverted regions. <sup>[32]</sup> .....	46
<b>Figure 25:</b> The intersection point between the parabolas in different regimes.....	46
<b>Figure 26:</b> IE offsets between a) P3HT:IEICO, b) P3HT:IT-4F. Where, $GDA^{**}$ is the optical bandgap of the acceptor, and BE is the binding energy.....	47

<b>Figure 27:</b> (from left to right) The molecular structure of PC60BM, PC70BM, and P3HT. <sup>[38]</sup> .....	49
<b>Figure 28:</b> Molecular structure of a) Rylene diimide, b) Fused-ring electron acceptor (FREA). <sup>[42]</sup> .....	50
<b>Figure 29:</b> Chemical structures of the investigated donor and acceptors materials.....	52
<b>Figure 30:</b> Energy levels diagram measured by PESA.....	52
<b>Figure 31:</b> IE values using PESA. Figures d, e, f, and g were taken from previous work. <sup>[30]</sup> .....	53
<b>Figure 32:</b> a) Energy level diagram of the device (inter)layers. b) Inverted device structure.....	54
<b>Figure 33:</b> ITO substrate.....	62
<b>Figure 34:</b> Final structure of OSCs.....	63
<b>Figure 35:</b> UV-vis absorption (absorbance) spectra of a) neat films, b) neat films (non-normalized), c) donor-acceptor blend films.....	66
<b>Figure 36:</b> Normalized absorbance and emission spectra and optical bandgaps indicated by the dashed vertical lines of a) P3HT, b) BT-CIC, c) IT-4F, d) IEICO, e) IEICO-4Cl, f) IEICO-4F, and g) O-IDTBR.....	68
<b>Figure 37:</b> Overlap of donor PL (normalized) and acceptor absorbance spectra indicating the possibility of energy transfer from the donor to the acceptors. ....	69
<b>Figure 38:</b> J-V curves of the best performance of P3HT:NFA based OSCs.....	70
<b>Figure 39:</b> Relation between the $V_{OC}$ and the optical bandgap between the HOMO of the donor and the LUMO of the acceptor. ....	72
<b>Figure 40:</b> External quantum efficiency (EQE) spectrum of P3HT:NFA OSCs. ....	73
<b>Figure 41:</b> Simulated device structure. ....	75
<b>Figure 42:</b> Extinction coefficients $k$ and refractive indexes $n$ of the active layers of a) P3HT:BT-CIC, b) P3HT:IT-4F, c) P3HT:IEICO, d) P3HT:IEICO-4Cl, e) P3HT:IEICO-4F, f) P3HT:O-IDTBR.....	76
<b>Figure 43:</b> a) Internal quantum efficiency (IQE) of P3HT:NFA OSCs, b) averaged IQE vs. IE offsets.....	77
<b>Figure 44:</b> Driving force $\Delta G^*$ and IE offset .....	78

**LIST OF TABLES**

<b>Table 1</b>	Optimization process of P3HT:BT-CIC.....	52
<b>Table 2</b>	Optimization process of P3HT:IT-4F. ....	53
<b>Table 3</b>	Optimization process of P3HT:IEICO .....	54
<b>Table 4</b>	Optimization process of P3HT:IEICO-4CL .....	55
<b>Table 5</b>	Optimization process of P3HT:IEICO-4F .....	55
<b>Table 6</b>	Optimization process of P3HT:O-IDTBR .....	56
<b>Table 7</b>	Figures of merit of P3HT:NFAs OSCs in order of decreasing IE offset. ....	67

## Chapter 1: Introduction

We are facing a massive growing demand for energy nowadays. Conventional energy sources such as fossil fuels have a negative environmental impact. Despite the low cost of fossil fuels compared with clean energy sources, the environmental pollution cannot be ignored as we are under the threat of a huge global warming. Therefore, we need to find alternative solutions that could have a positive environmental impact. Renewable energy sources such as solar, geothermal, biomass, hydroelectric, wind, and ocean energies (Figure 1)<sup>[1]</sup> can produce electricity with less pollution as a result global warming will decrease accordingly. Sunlight and hydroelectric energy can generate clean energy with minor adverse environmental impact compared with conventional energy sources. Generally, it is critical to distinguish which renewable energy source could maximize the outcome and minimize the energy consumption.<sup>[2]</sup> On the other hand, renewable energy can be affected by several factors: natural disasters and environmental fluctuations. Geothermal energy, for example, can be disturbed by earthquakes as well as stability and cost can be a significant problem in solar energy.<sup>[3]</sup>

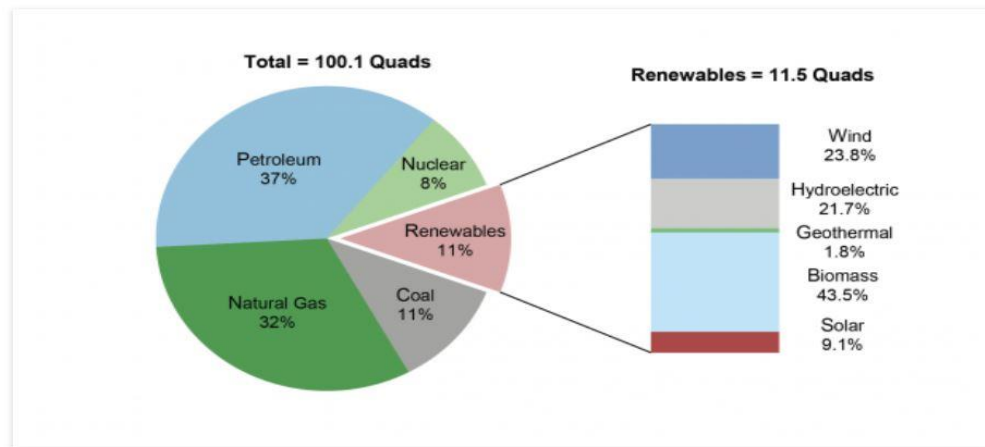


**Figure 1:** Renewable and total energy consumption (2019).<sup>[4]</sup>

Solar energy is an abundant source on our planet. However only 0.004% of this energy is extracted from photovoltaic (PV) panels due to the high cost of these panels. Actually, using PV panels cost more than burning fossil fuels. Researchers directed toward lower cost technologies such as organic photovoltaic (OPV). OPVs have a theoretical potential to produce electricity at lower cost compared to PV panels. However, the efficiency of OPVs remains a major challenge in this field due to energy losses and low carrier mobility. In addition, exciton diffusion length used to be a problem but it has been solved by the invention of bulk-heterojunctions. OPVs are developing over the years, starting with very low power conversion efficiency (PCE), and now reaching over 18% [7] PCE still lower than multi-crystalline Silicon 23% PCE but developing very fast.

The photovoltaic effect was discovered in 1839 by a Edmond Becquerel when he noticed that a cell containing conducting solution sandwiched between two metal electrodes generated electricity when it was exposed to light.<sup>[5]</sup> Three years later, William Adam and Richard Evans conducted experiments on Selenium using the photovoltaic effect. In 1905 Albert Einstein played a major role in explaining the photoelectric effect and how the light carries energy, thus brought the world's attention to solar energy and its features.<sup>[5]</sup>

There are many types of PV technologies such as: monocrystalline silicon, polycrystalline silicon, and thin-films. Moreover, there are some emerging technologies such as organic solar cells, perovskite cells, and quantum dots.<sup>[6]</sup> Figure 2, shows the development of these cells over the years.

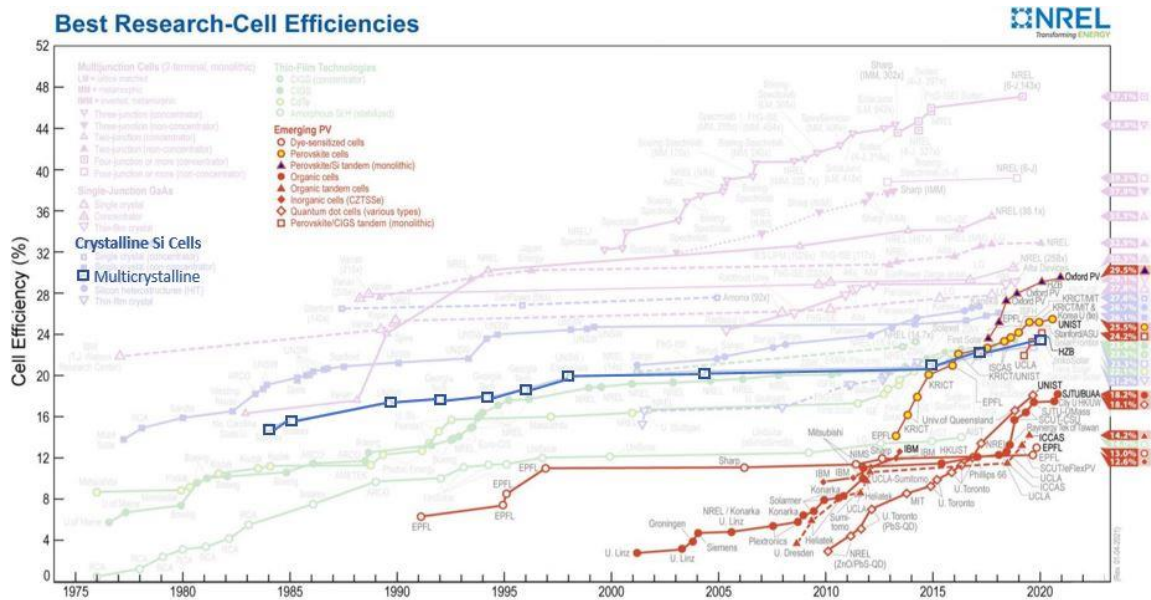


**Figure 2:** Growth of efficiencies for a range of photovoltaic technologies.<sup>[7]</sup>

In addition to conventional applications, there are some additional ones for OPV. For example, black and opaque panels are not practical solutions to cover buildings and windows, mainly due to the architecture development nowadays. OPVs and their colours diversity solve this problem because they can be made transparent by generating electricity mostly with non-visible part of light thanks to their large absorption tunability.

OPVs consist of many interlayers, each layer has a specific function that helps improving the overall efficiency of OPVs. The most important layer is the photoactive layer which consists of two materials electron donor and electron acceptor. Charge transfer between donor and the acceptor can be controlled by the electron affinity (EA) and ionization energy (IE).

The scope of this thesis is to investigate the effect of the ionization energy offsets on the performance of OPVs. Understanding the relation between IE offsets and charge generation is very important in order to improve the power conversion efficiency of organic solar cells and this improvement would increase the reliance on renewable energy. OSCs are suffering from energy losses, charge recombination, and many more factors that can affect the exciton-charge separation. Therefore, it is very difficult to determine which factor or factors can be affected by increasing or decreasing the IE offsets. This work is based on a previous investigation of IE offsets but with smaller values compared with this thesis. This would give a very valuable comparison between large and small IE offsets and thus more understanding of the impact of IE offsets on OPVs.

## Chapter 2: Theoretical Background

### 2.1 Solar radiation and photovoltaic effect / efficiency

The solar resource, sunlight, or solar radiation correspond to electromagnetic radiation emitted by the sun.<sup>[8]</sup> The available solar power is quantified by the solar irradiance, expressed in unit of Watt per square meter ( $\text{W}/\text{m}^2$ ).<sup>[9]</sup> Solar radiation under the earth's atmosphere covers three main regions: Near-infrared (NIR), Visible (VIS), and Ultraviolet (UV) (figure 3).

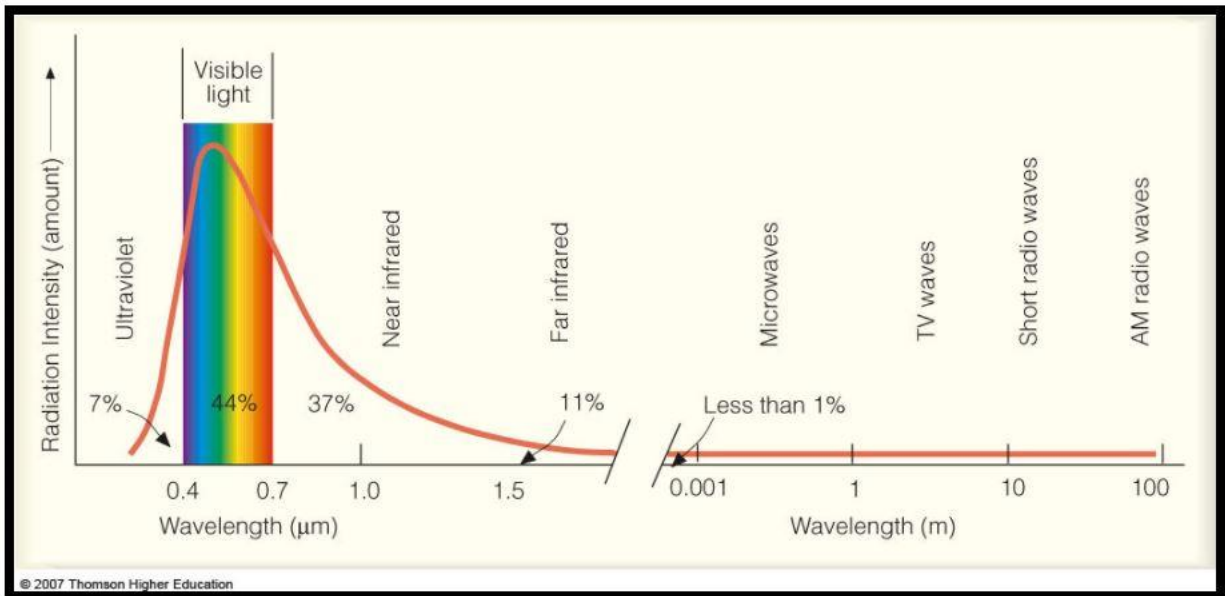


**Figure 3:** Solar radiation spectrum.<sup>[10]</sup>

The photovoltaic effect is a photophysical phenomenon that explains the generation of electricity by absorbing light. In order for light to be absorbed and generate photocurrent in PV panels the energy of photons must be larger than the bandgap of the semiconductor. The photon energy is related to its wavelength and each photon correspond to a certain wavelength and frequency (Equation 1).<sup>[11]</sup>

$$E_{\text{photon}} = \frac{hc}{\lambda} = h\nu \quad (1)$$

Where  $h$  is Planck's constant,  $\lambda$  is the wavelength of the photon,  $c$  is the speed of light, and  $\nu$  is the light frequency. <sup>[11]</sup>

## 2.2 Organic Solar Cells (OSCs)

Organic solar cells with  $\pi$ -conjugated polymers and small molecules (figure 4) have gained academic and industry attraction due to many factors, for instance, electronic properties, flexibility, low cost, and processing methods.

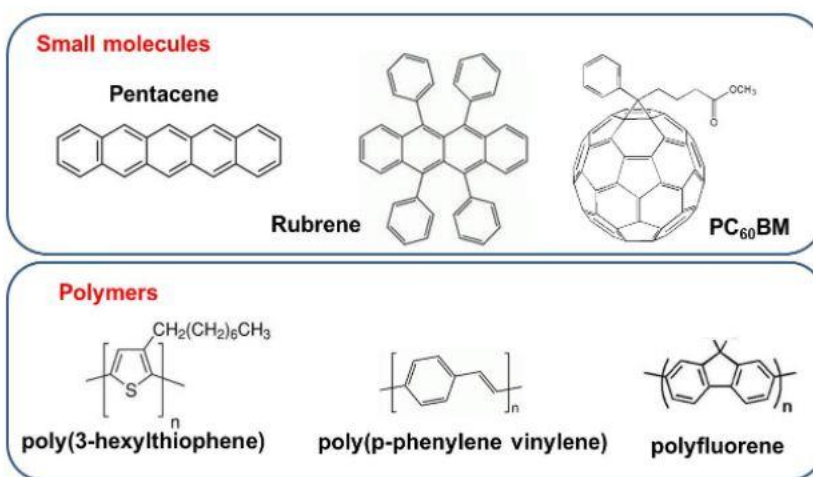
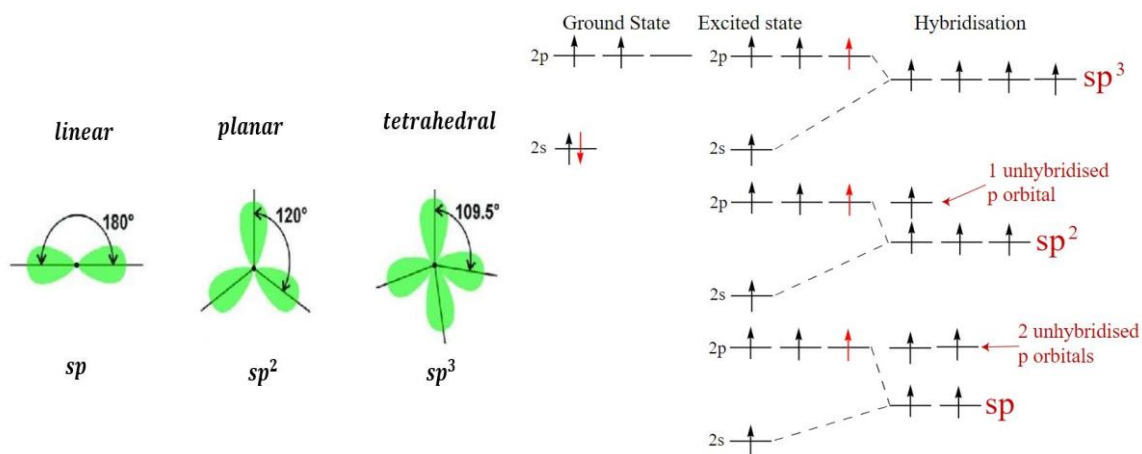


Figure 4: Molecular structure of conjugated polymers and small molecules. <sup>[12]</sup>

Although organic solar cells have lower power conversion efficiency (PCE) and lifetime than inorganic solar cells, they are flexible and transparent compared to inorganic solar cells. The semiconductors used for organic solar cells can be either polymers or small molecules. <sup>[13]</sup>

### 2.2.1 Organic Semiconductors

Conjugated polymers and small molecules have a conjugated  $\pi$ -electron system responsible for the semiconducting properties in the OSCs. The semiconducting materials in OSCs are carbon-based. The electron configuration of the carbon atom explains the chemical bonds in organic semiconducting materials. The carbon atom (C) has six electrons, so the electron configuration is  $1s^2 2s^2 2p^2$ . The carbon atom has four valence electrons that form covalent bonds with other atoms to complete the shell and reach stability. In order to combine orbitals, the hybridization concept needs to be introduced. Hybridization is combining atomic orbitals to form a new hybrid orbital to form chemical bonds. In the electron configuration of the carbon atom, the hybridization orbitals could be  $sp$ ,  $sp^2$ , and  $sp^3$  (Figure 5).  $sp^2$  hybrid-orbital has a planar geometry with  $120^\circ$  bond angles, thus combine one (s) orbital with two (p) orbitals, leaving one non-hybridized orbital ( $p_z$ ). The electronic configuration of  $sp^2$  is  $2s^1 2p_x^1 2p_y^2$ . As a result, this hybridization creates two types of covalent bonding: sigma bond ( $\sigma$ ) and pi bond ( $\pi$ ). Sigma bond is strong because it is formed by overlapping the hybridized orbitals of  $sp^2$ . In contrast to sigma bond,  $\pi$  bond is weaker because it is formed by overlapping the non-hybridized orbital  $p_z$ . Moreover,  $\pi$ -bond is responsible for charge transfer due to their delocalization.<sup>[14]</sup>



**Figure 5:**  $sp$ ,  $sp^2$ , and  $sp^3$  hybrid orbitals.<sup>[15]</sup>

Conjugated systems consist of several alternating single and double bonds. Moreover, increasing the number of  $\pi$ -bonds decreases the bandgap of the conjugated polymer. The number of atoms involved in the conjugated system is called conjugation length. In conjugated systems the energies of the ground state and the excited state are closer to each other. As a result, lower photon energy is needed in order to excite the electrons at the ground state and this explains their absorption in the visible region or NIR if the conjugation length is very long.<sup>[14]</sup>

In organic semiconductor charge transport takes place between highest occupied molecular orbital (HOMO) and lowest unoccupied molecular orbital (LUMO). These orbitals are separated by a distance called forbidden gap or bandgap. HOMO is generated by overlapping  $\pi$ -orbitals, while LUMO is formed by overlapping anti-bonding  $\pi^*$ -orbitals (Figure 6). At least energy equal to the bandgap is required for exciting electron from HOMO to LUMO, thus leaves a positive charge particle (hole) at the HOMO.<sup>[14]</sup>

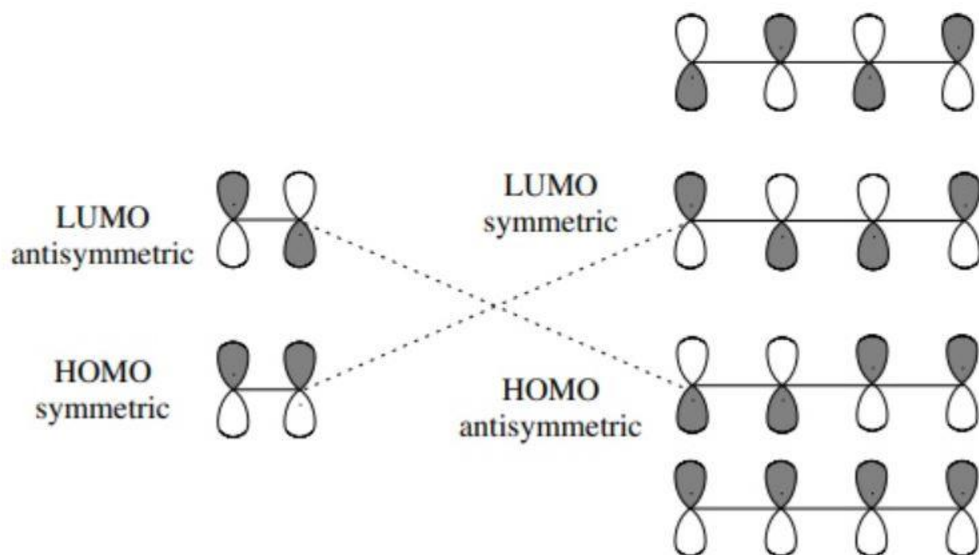


**Figure 6:** HOMO and LUMO formation.<sup>[16]</sup>

In organic semiconductors Van-der-Waals (VdW) force takes place between the molecules, and this leads to localization in the electronic states but the delocalization of orbitals does not extend to the next molecule. Therefore, charge carriers move by hopping between those localized states. In contrast to organic semiconductor, inorganic semiconductors atoms are bond by strong covalent bonds that enable large scale delocalization. This large delocalization leads to the formation of energy bands: valence band and conduction band separated by forbidden band or bandgap. In addition to the bands differences between organic and inorganic semiconductors, the dielectric constant in inorganic semiconductor is larger compared to organic semiconductor, thus low binding energy between the hole at the valance band and the electron at the conduction band (hole-electron pair). Therefore, hole-electron pair (exciton) dissociation is much easier compared to small dielectric constant in organic semiconductors. Exciton dissociation to free charges in organic

semiconductors require energy more than 0.4 eV, because the binding energy of Frenkel exciton which appears in organic semiconductor is 0.2-0,4 eV. <sup>[14][15]</sup>

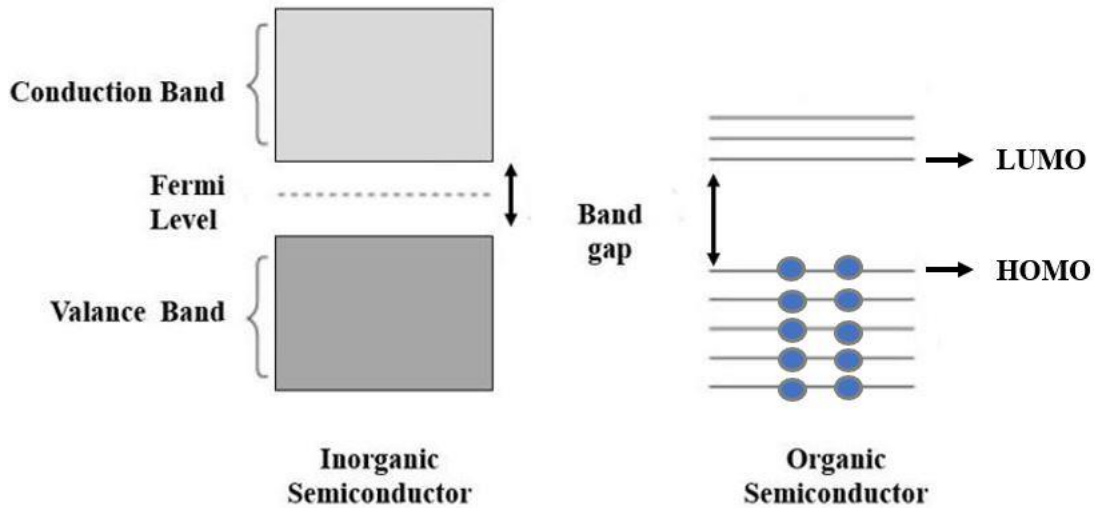


**Figure 7:** Energy bands diagram of Inorganic and Organic semiconductors.

### 2.2.2 Structures of organic photovoltaic devices

There are three main structures of organic photovoltaics (OPVs): single layer, bilayer, and bulk heterojunction (ordered or disordered), as can be shown in (figure 8).<sup>[17]</sup> First, a single layer device (figure 8-a) is the simplest structure composed of a conjugated polymer layer sandwiched between two different electrodes with different work functions. This difference creates a built-in electric field that can generate a driving force for photogenerated holes and electrons toward the electrodes. However, this electric field is not strong enough to overcome electron and hole electrostatic binding. Therefore this structure has very low external quantum efficiency (EQE) and power conversion efficiency (PCE).<sup>[17]</sup> Second, the bilayer structure (figure 8-b) comprises two sublayers in the photoactive layer, which are doner/acceptor layers. The thickness of the active layer plays a vital role in the number of absorbed photons. Less than 100 nm could not be efficient in absorbing photons. However,

the fact that only excitons near the donor/acceptor interface ( $\sim 10$  nm) can be dissociated to free charges limits the use of this structure.<sup>[17]</sup> Finally, bulk heterojunction (BHJ) structure (figure 8-c) composed of mixed donor and acceptor, therefore creates large interfacial area more than bilayer structure. A large interfacial area enhances the exciton dissociation effectiveness. Also, phase separation should make an interdigitated network to help charge carriers to dissociate, and thus will reduce charge recombination as well as increasing the internal quantum efficiency (IQE).<sup>[17]</sup>

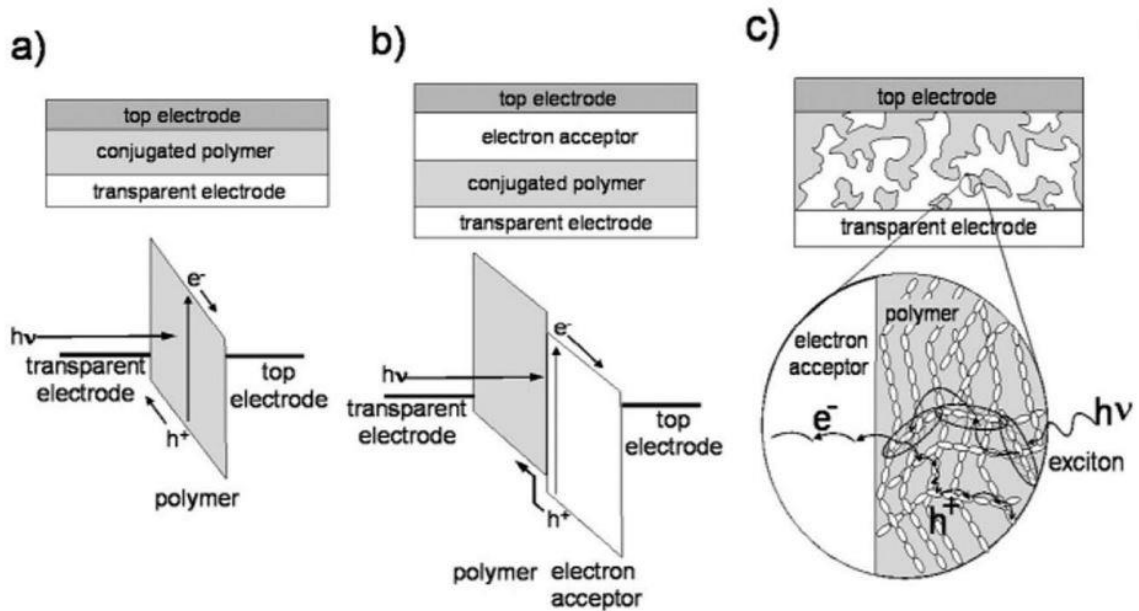


**Figure 8:** Different device structures a) single layer b) bilayer and c) bulk heterojunction (BHJ).<sup>[18]</sup>

### 2.3 Working mechanism of organic photovoltaics

OPVs working mechanism is schematically composed of four main processes as can be schematically illustrated in (figure 9) which are: a) photon absorption and exciton generation, b) exciton diffusion, c) exciton dissociation and charge separation, and d) charge transport and extraction.<sup>[19]</sup>

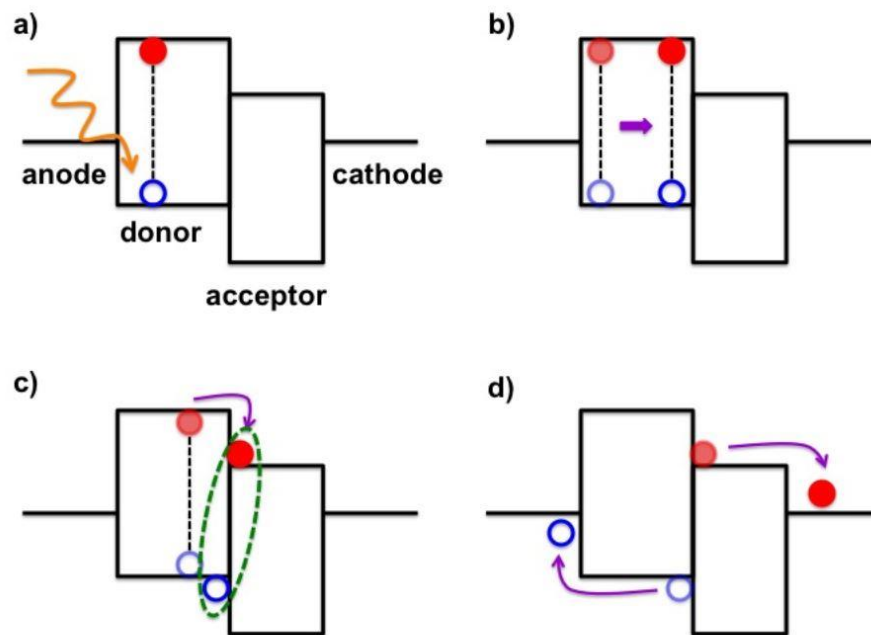


**Figure 9:** OPVs working mechanism.<sup>[20]</sup>

#### 2.3.1 Photon absorption and exciton generation

When the photon got absorbed, an electron is promoted from the HOMO to the LUMO of the absorber, leaving a positively charged particle (hole) at the HOMO of the absorber. Hole and electron are attracted to each other by Coulomb force (Equation 2), thus generating an hole-electron pair called exciton.<sup>[19]</sup>

$$F = k \frac{q_1 q_2}{r^2} \quad (2)$$

Where,  $F$  is the electric force,  $k$  is Coulomb constant,  $q_1 q_2$  are the charges, and  $r$  is the separation distance between the charges.

### 2.3.2 Exciton diffusion

After exciton generation, the movement of excitons is called exciton diffusion. Frenkel excitons move in organic semiconductors via a hopping mechanism. The diffusion length is the average distance that the exciton can travel before it decays back to the ground state. Diffusion length can be expressed by this equation:

$$L_D = \sqrt{D\tau} \quad (3)$$

Where,  $D$  is the average distance of the exciton, and  $\tau$  is lifetime of the exciton.

Furthermore, in order for exciton to reach the interfacial area between donor and acceptor materials in BHJs, excitons must have enough diffusion length which is in the range of (10-20) nm otherwise, exciton recombination takes place.<sup>[21]</sup>

### 2.3.3 Exciton dissociation and charge separation

After exciton diffusion, exciton reaches the interface between the donor and the acceptor. Therefore, charge transfer (CT) state is created across the interface between the HOMO of the donor and the LUMO of the acceptor. In order to have free charges, (CT) state excitons must be separated before they recombine again by geminate recombination.<sup>[21]</sup>

### 2.3.4 Charge transport and extraction

A built-in electric field created due to the differences between the work functions of the electrodes contributes to helping charges drift towards their respective electrodes. Moreover, charge separation must be followed by fast charge extraction to prevent non-geminate recombination.<sup>[19]</sup> Also, the high mobility of charge carriers can contribute to minimizing the non-geminate recombination.

## 2.4 Characterization of organic solar cells

### 2.4.1 Current-Voltage Characterization

There are four essential parameters in the current-voltage (J-V) curve: the open-circuit voltage ( $V_{OC}$ ), the short circuit current density ( $J_{SC}$ ), the fill factor (FF), and the power conversion efficiency (PCE). When there is no current flow in the solar cell,  $V_{OC}$  is the voltage in the cell. When there is no voltage applied in the solar cell,  $J_{SC}$  is the current in the cell, which can be illustrated (figure 10).<sup>[22]</sup> The maximum power point (MPP) is the point of the curve for which the product of the voltage and the current is maximized. The fill factor can be defined as the ratio of the maximum power over the product of  $V_{OC}$  and  $J_{SC}$ , as shown in (equation4).<sup>[22]</sup>

$$FF = \frac{V_{MPP} \times J_{MPP}}{V_{OC} \times J_{SC}} \quad (4)$$

The fill factor can illustrate how close the experimental solar cell is to the ideal J-V curve, which is a rectangular shape (grey area in figure 10).

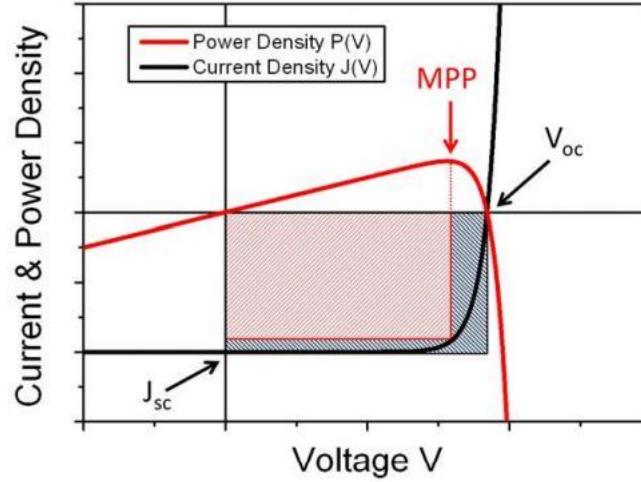


**Figure 10:** Schematic of J-V curve (black line) and power voltage (red line) of a solar cell under illumination.<sup>[23]</sup>

The power conversion efficiency can be defined as the electric output power divided by the light input power (equation 5).

$$PCE = \frac{V_{MPP} \times J_{MPP}}{p_{in}} = \frac{FF \times V_{OC} \times J_{SC}}{p_{in}} \quad (5)$$

Where ( $p_{in}$ ) is the input power generated by the solar simulator. When, the solar simulator is set to 1 sun  $p_{in}$  is equal to ( $1000 \text{ W/m}^2$ ).

### 2.4.2 External quantum efficiency (EQE)

External quantum efficiency EQE calculates the number of charge carriers can be collected from the cell over the number of incident photons.<sup>[24]</sup>

$$EQE = \frac{\text{electrons}}{\text{incident photons}} \quad (6)$$

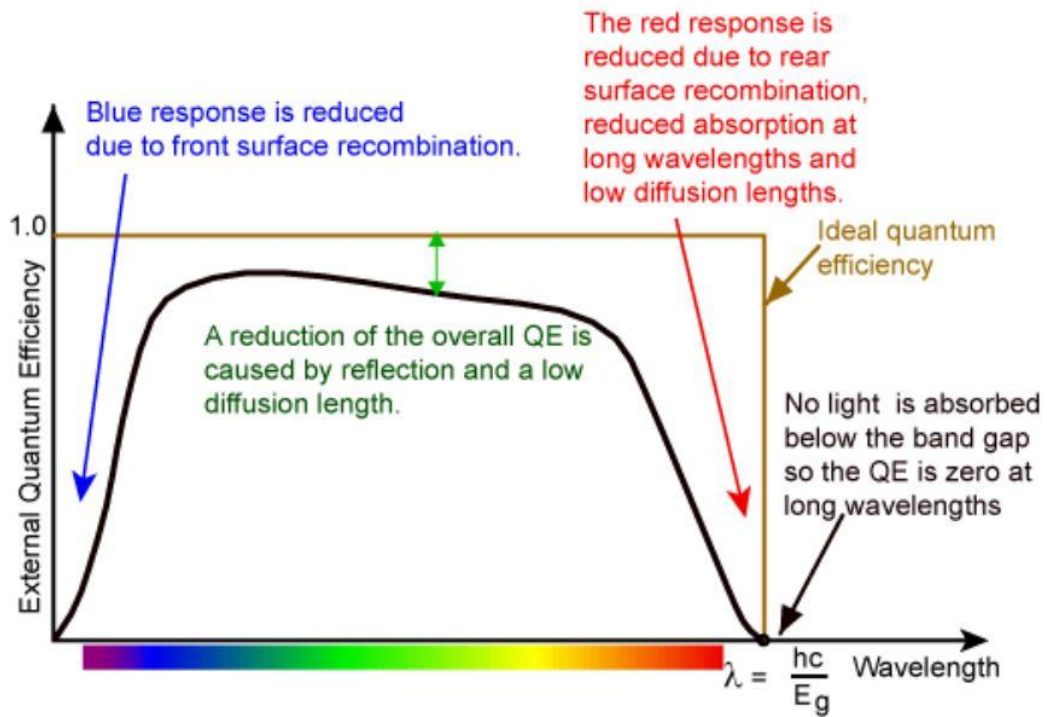


**Figure 11:** Comparison between ideal and experimental EQE spectra for Si solar cell  
[25]

The ideal EQE spectra has a rectangular shape, but loss processes such as parasitic absorption of interlayers and incomplete photon absorption of the photoactive layer in certain spectral regions can reduce the EQE. The internal quantum efficiency (IQE) provides deeper insight into losses occurring after absorption of photons by the photoactive layer such as incomplete exciton-to-charge conversion and charge carrier recombination.

### 2.4.3 Internal quantum efficiency (IQE)

Unlike the EQE, IQE calculates how many charge carriers can be collected over how many photons are absorbed by the photoactive layer.

$$IQE = \frac{\text{electrons}}{\text{absorbed photons}} \quad (7)[24]$$

Charge recombination and slow charge extraction in the active layer of OSCs have a negative impact on the IQE.

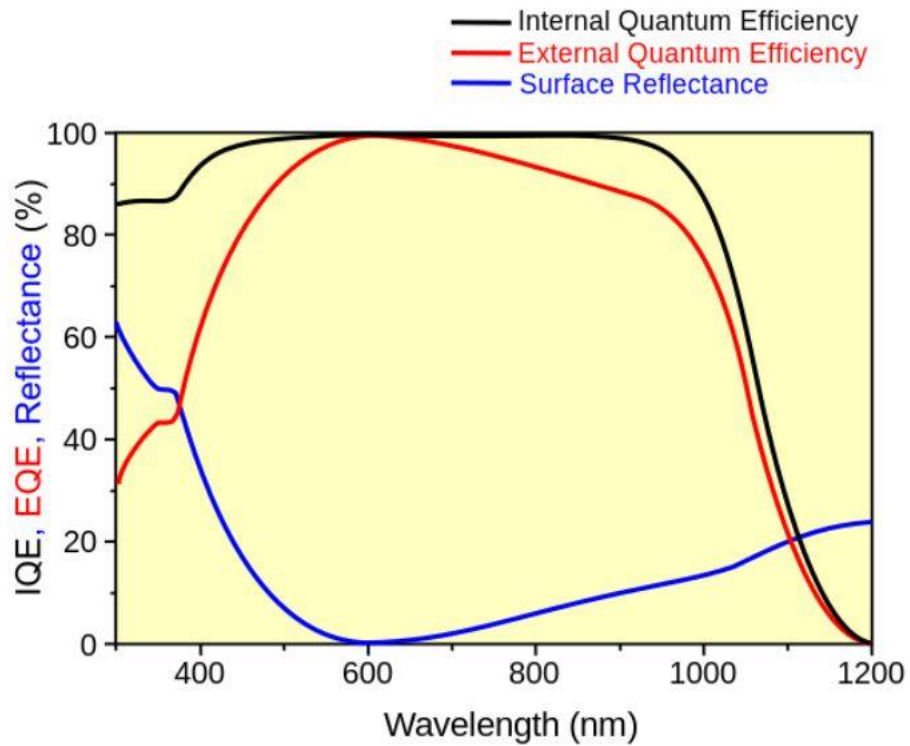


**Figure 12:** IQE, EQE, and reflectance spectra.<sup>[24]</sup>

## 2.5 Preparation of organic solar cells

### 2.5.1 Photoactive materials

The most critical layer in the BHJ based OSCs is the photoactive layer. It is a mixture of electron donor and acceptor materials. These materials can be evaporated, or dissolved in various solvents and thus generate a photoactive solution that can be printed or coated to form a photoactive layer (solvent choice and coating mechanism will be discussed). Photoactive materials can be conjugated polymers or small molecules (donors and acceptors). Furthermore, acceptors can be fullerene derivatives or more recent non-fullerene acceptors (NFAs). (FAs and NFAs will be discussed in section 2.7.2 and 2.7.3)

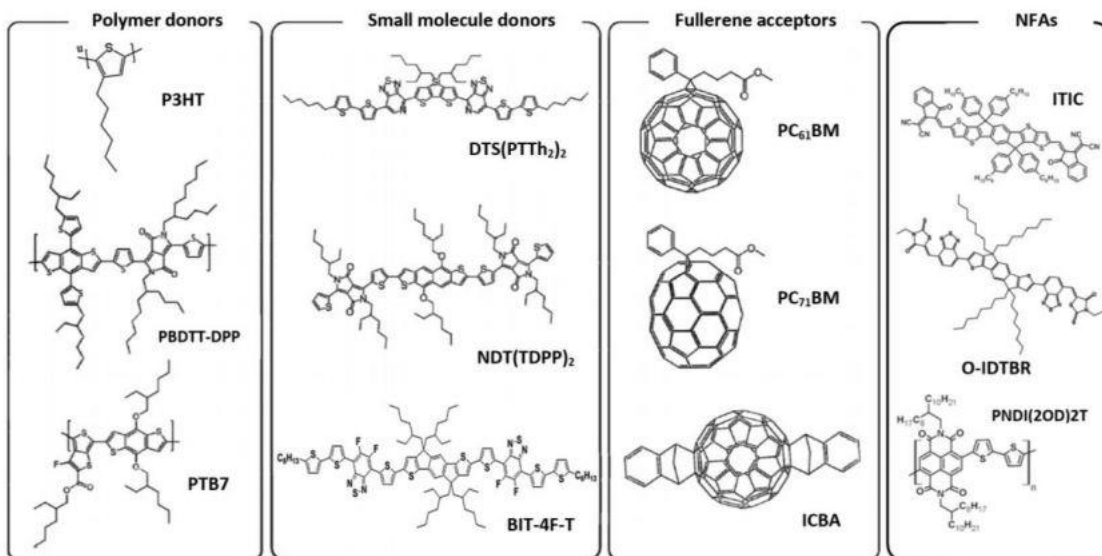


**Figure 13:** Chemical structures of donor and acceptor materials in OPVs.<sup>[22]</sup>

### **2.5.2 Solvents**

The choice of solvents is one of the important factors in the photoactive solution. If the material does not dissolve very well in the solvent, the concentration of the solution is affected. Chlorinated solvents such as chlorobenzene (CB), dichlorobenzene (DCB), and chloroform (CF) typically dissolve many organic materials well. Moreover, additives like 1,8-diodooctane (DIO), 1,8-octanedithiol, 1-chloronaphthalene (CN), 1-phenylnaphthalene (PN), and others are often added and play an essential role in controlling the morphology of the donor and acceptor in the photoactive layer. Changing the layer's morphology influences the PCE of the solar cell.<sup>[26]</sup>

### **2.5.3 Coating techniques**

Many coating or deposition methods can be used in OPVs fabrication, for instance, dip coating, flow coating, spray coating, and spin coating. Among these techniques, spin coating is the most frequently used technique for small area laboratory applications. This is due to several reasons including high-speed processing and control of the thickness of the films by changing spinning speed and time as well as concentration of the solution. However, more than 90% of the material is lost which is one of the biggest problems in the spin coating technique. Four main processes explain what happens during the spin coating process: deposition, spin-up, spin-off, and evaporation (figure 14).<sup>[27]</sup>

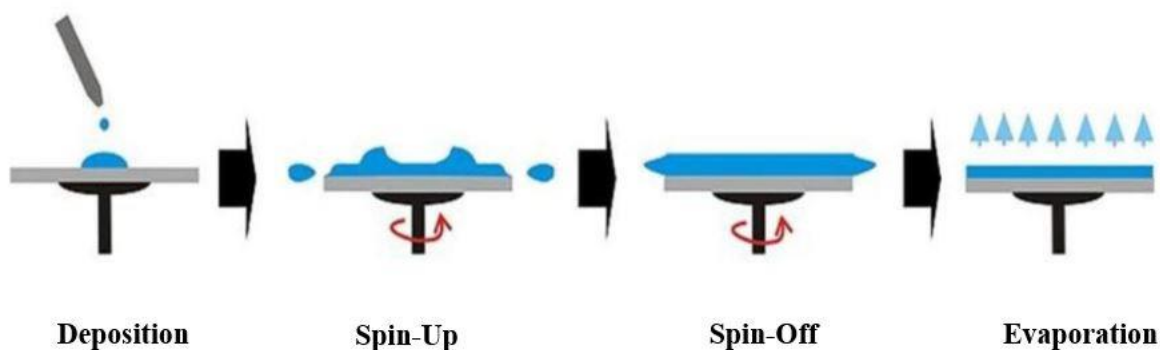


**Figure 14:** Spin coating processes.<sup>[28]</sup>

## 2.6 Energy levels and their determination

### 2.6.1 Electron affinity and ionization energy

Each organic molecule has certain electron affinity (EA) and ionization energy (IE) characteristics. Electron affinity can be described as the energy change upon gaining an extra electron. Moreover, electron affinity is closely related to the LUMO of the molecule. In contrast to EA, ionization energy is the energy required to take away one electron, and it is related to the HOMO of the molecule. Note that some references refer to IE as Ionization potential (IP). EA and IE are critical material properties for OSC applications<sup>[29]</sup> For instance, IE controls the ability of a molecule to accept holes (donate electrons). Similarly, EA controls the ability of the molecule to accept electrons. Furthermore, they control charge injection from the electrodes and charge extraction to the electrodes.

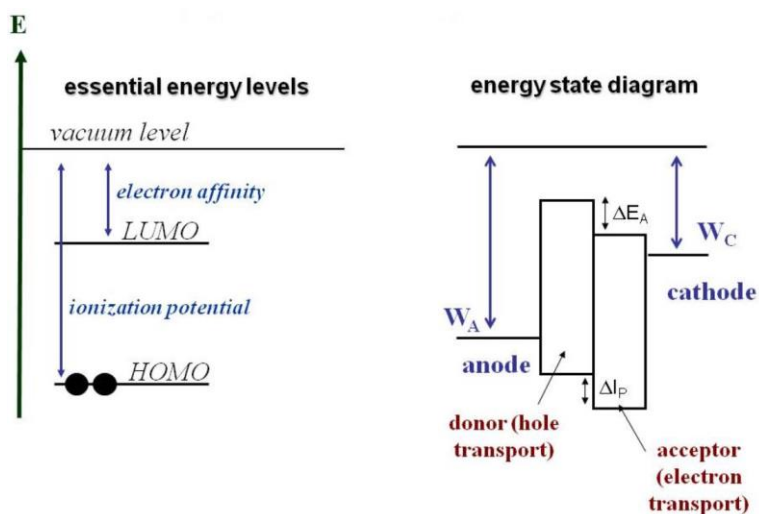


**Figure 15:** Energy levels diagram,  $W_A$  is the work function of the anode,  $W_C$  is the work function of the cathode in open circuit conditions.<sup>[29]</sup>

In order to separate the charges, the IE of the donor and the EA of the acceptor must be chosen in a way that the CT state exciton binding energy at the interface between donor and acceptor can be overcome. Thereafter, the electric field created due to the differences in the work-functions of the electrodes drives the charges to their respective electrodes for extraction.<sup>[29]</sup> A type II heterojunction is the way to obtain such energetic situation.

For photovoltaics, the most favorable HOMO-LUMO distribution structure is a type II heterojunction (figure 16). The HOMO of the donor is shallower than the HOMO of the acceptor. Similarly, the LUMO of the donor is higher than that of the acceptor. Still, charge separation can be hampered and charge recombination could occur in this structure, but charge transfer is facilitated compared to a type I heterojunction. In the type I heterojunction electron and hole are both transferred to the acceptor and thus recombination of an exciton takes place in the acceptor, while in type II heterojunctions the charges remain separated.

The difference between the IE of the acceptor and the IE of the donor ( $\Delta$ IE, IE offset) helps to overcome the (acceptor) exciton binding energy and it drives the charge transfer process. At the same time, IE offsets should not be very large, because this decreases the CT state energy and thus the device  $V_{OC}$ . Furthermore, charge transfer could potentially be slowed and less efficient for very large offsets (as discussed in 2.6.3).

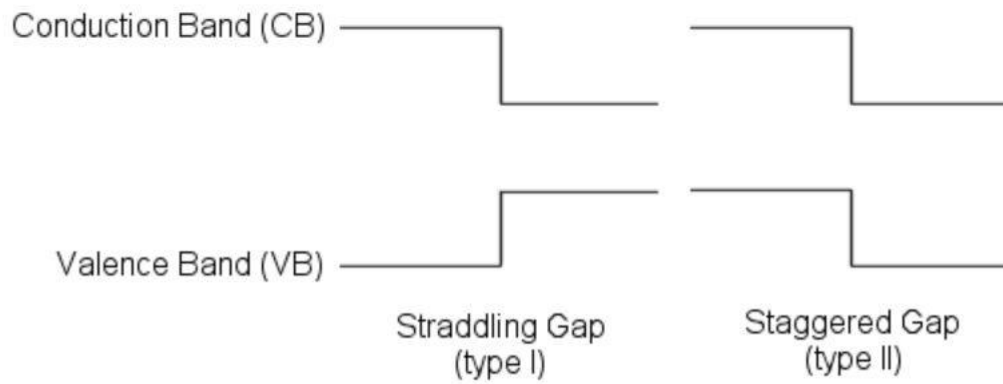


**Figure 16:** Semiconductor heterojunction energy band diagram.<sup>[29]</sup>

### 2.6.2 Role of ionization energy level offsets

Theoretically, both IE and EA offsets at the interface contribute to the exciton dissociation process: electrons can transfer from higher to lower EA levels and holes can transfer from lower to higher IE levels. The first path is controlled by EA offsets and the second path by IE offsets.<sup>[30]</sup>

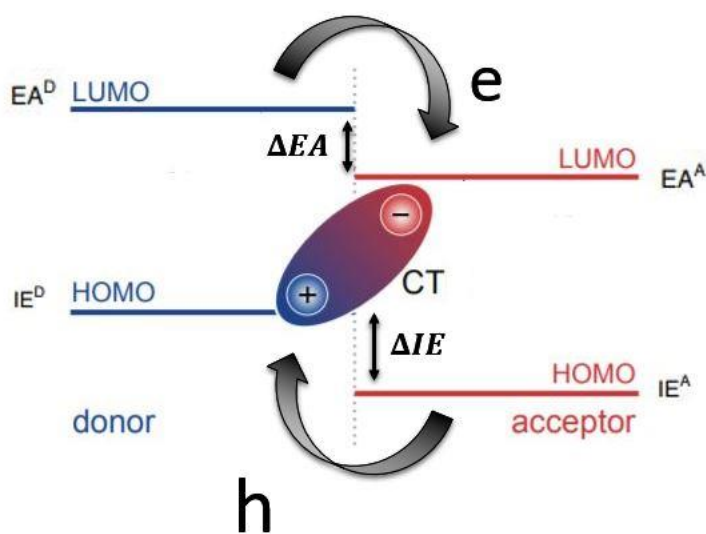


**Figure 17:** Energy levels schematic shows electron and hole transfer.  $\Delta IE$  is the IE offset, and  $\Delta EA$  is EA offset.<sup>[21]</sup>

However, recent studies demonstrated that energy transfer from the donor to the acceptor (known as Förster Resonance Energy Transfer (FRET)) followed by hole transfer from the acceptor to the donor occurs in NFA-based OSCs. This makes the EA offset less important as a driving force for charge transfer.<sup>[30]</sup>

In fact, generally the IQE seems to increase with the IE offset. (Figure18-b)<sup>[30]</sup> Electron transfer processes in DA systems can be described by Marcus theory (discussed below). Figure 18 shows different systems with different IE offsets and how changing the offsets changes the IQE of these NFA-based systems.

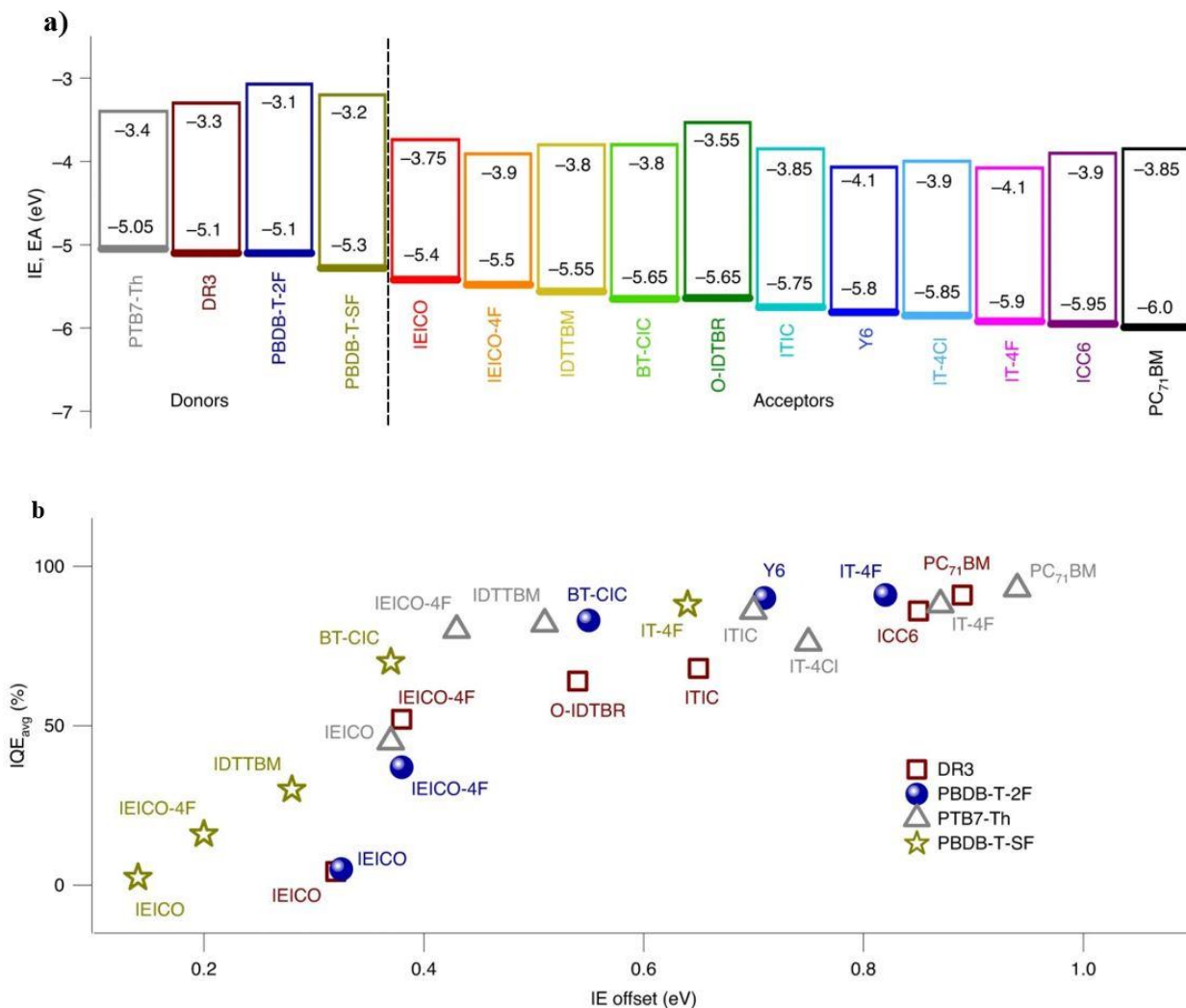


**Figure 18:** Energy levels of different materials. b) Relation between IE offsets and averaged IQE, symbols are for D:A system, D indicated in the legend and A written next to the symbol.<sup>[30]</sup>

The fact that energy levels are not flat at the interface and that there is an energy level bending (B) at the interface between the donor and acceptor (Figure 19) effectively decreases the IE offsets at the interface in NFA-based systems.<sup>[30]</sup>

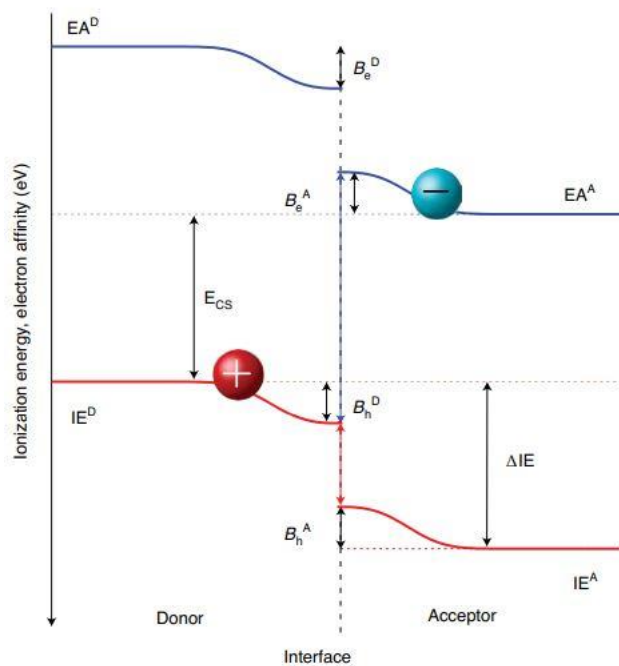


**Figure 19:** Band bending at the interface between donor and acceptor.<sup>[30]</sup>

Energy level bending increases the interfacial CT state energy and reduces the driving force for exciton-to-CT state conversion. In order for CT state dissociation to occur and to generate separate charges, the charge separation energy  $E_{CS}$  has to be lower than the CT state energy.<sup>[30]</sup>

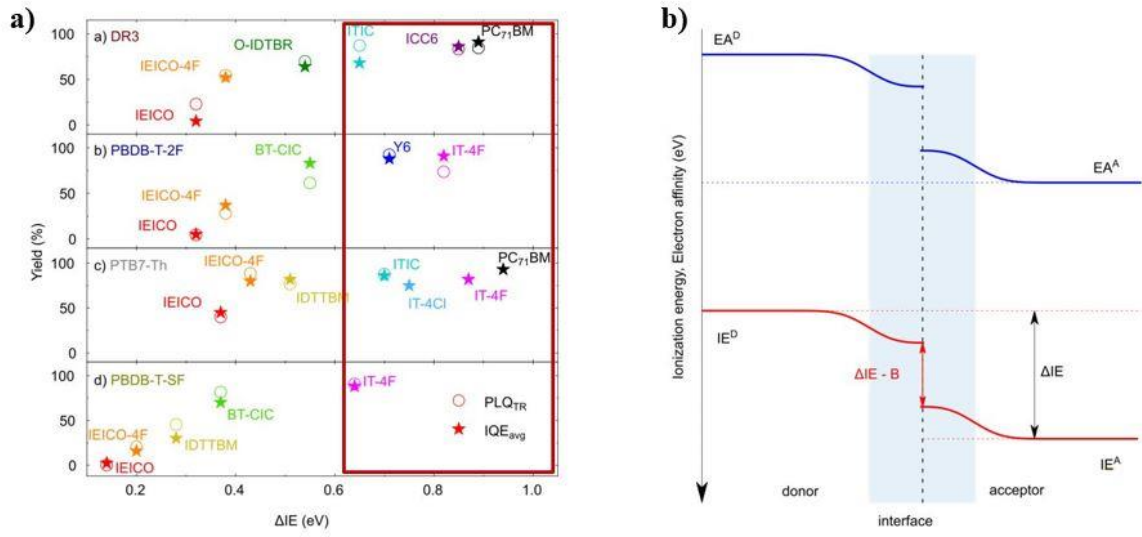


**Figure 20:** a) Relation between PLQ and IQE vs. IE offsets b) Band bending (B) for large IE offsets.<sup>[30]</sup>

Figure 20-b) shows the situation in a system where the IE offset is large enough and thus there is enough driving force to transfer the hole from the acceptor to the donor, consequently efficient hole transfer occurs, explaining why some systems have a very high IQE and efficient exciton quenching (as evidenced by time-resolved photoluminescence quenching PLQ<sub>TR</sub> (figure 20-a)).<sup>[30]</sup>

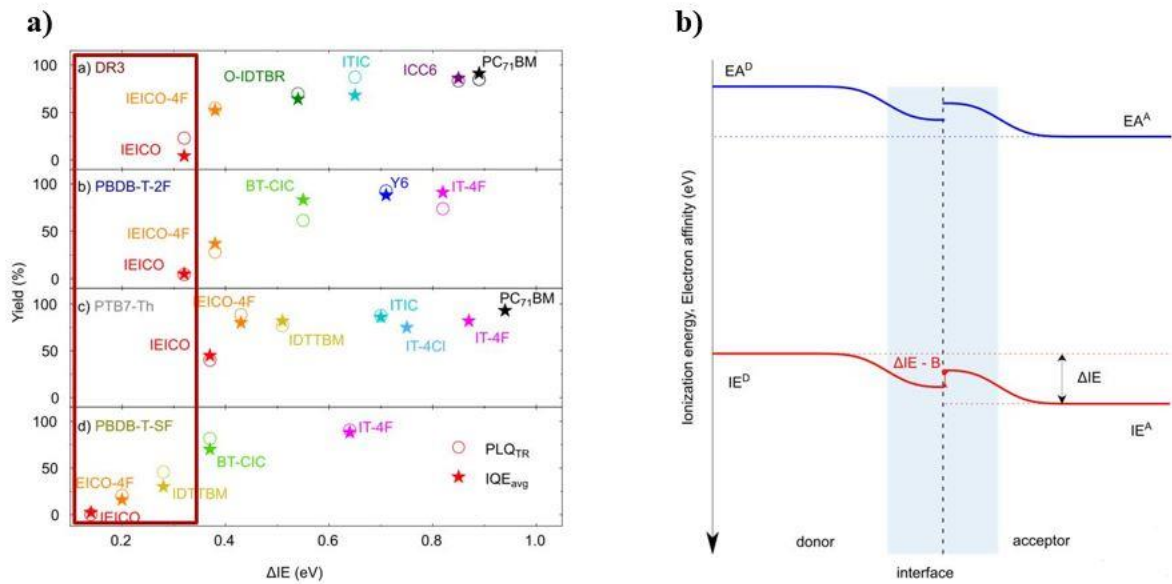


**Figure 21:** a) relation between PLQ and IQE against IE offsets b) band bending (B) with large IE offsets.<sup>[30]</sup>

In contrast to large IE offset systems, (figure 21) shows the case of small IE offsets. In small IE offset systems, there is an energy barrier at the interface between donor and acceptor (Figure 21-b), therefore hole transfer is impeded and low IQE is obtained. For this reason, a minimum driving force between 0.3 eV-0.5 eV<sup>[30][31]</sup> is suggested to guarantee efficient hole transfer between acceptor and donor.<sup>[30]</sup>

The IE can be determined by several techniques and spectroscopies such as Photoemission Spectroscopy in Air (PESA), Ultraviolet Photoelectron Spectroscopy (UPS), and Cyclic Voltammetry. EA can be determined by Inverse Photoemission Spectroscopy (IPES).<sup>[30]</sup>

### 2.6.3 Marcus Theory

In 1950, Rudy Marcus provided a theoretical model to describe electron transfer processes. Marcus explained the electron transfer rate from an electron donor to an electron acceptor.<sup>[33]</sup> Marcus considered only the electron transfer in the outer sphere of the donor and acceptor, which means the change is only in the charge (electronic state) of the donor and acceptor and there is no structural change (vibrational state). Later N.S Hush extended Marcus model by including the inner sphere electron transfer process, which changes the geometry or the coordination of the shells of donor and acceptor.<sup>[32]</sup>

The charge transfer process is fundamental to exciton dissociation, it creates a charge transfer exciton at the interface between the two semiconductors. Moreover, this process is very fast, it occurs in about 100 fs.<sup>[23]</sup>

The transfer of an electron from an excited donor state ( $D^*$ ) to an acceptor (A) in the ground state can be represented as,  $D^*A \rightarrow D^+A^-$ . The D-A parabola (Figure 22) represents the potential energy surface of the system's ground state. The  $D^*A$  parabola represent the potential energy surface before charge transfer (excitonic state). The  $D^+A^-$  represents the potential surface energy after the charge transfer process (CT state). The potential energy of the donor and acceptor are plotted against the generalized reaction coordinate, which represents the nuclear configuration and the polarization of the environment of these systems.<sup>[23]</sup> To achieve energy conservation between the parabolas, the electronic energy levels of  $D^+A^-$  and  $D^*A$  have to be similar, which means the electron transfer will occur roughly at the crossing point between the two parabolas.

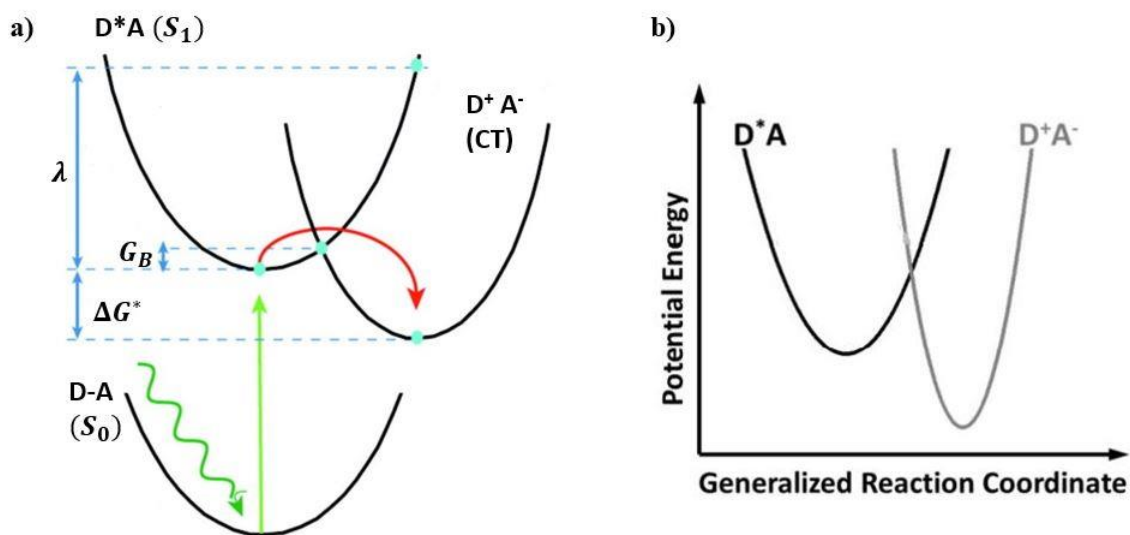


**Figure 22:** Potential energy surfaces of donor and acceptor.<sup>[23][34]</sup>

Figure 22 shows the energies of these systems, the excited and charge transfer states are energetically separated by the driving force,  $\Delta G^* = G_{D^*A} - G_{D+A^-}$ . In order for charge transfer to occur, the systems need to overcome the energy barrier  $G_B$ :

$$G_B = \frac{(\lambda + \Delta G^*)^2}{4\lambda} \quad (8)$$

where  $\lambda$  is the reorganization energy: the energy that the system would have in the  $D^*A$  state (on the  $D^*A$  parabola) if its reaction coordinates were those of the relaxed CT state (bottom of the  $D+A^-$  parabola).  $G_x$  is the intersection between the parabolas, where the charge transfer takes place as it represents where  $D^*A$  and  $D+A^-$  have the same energy value, all the energy described are Gibbs free energies.<sup>[23]</sup>

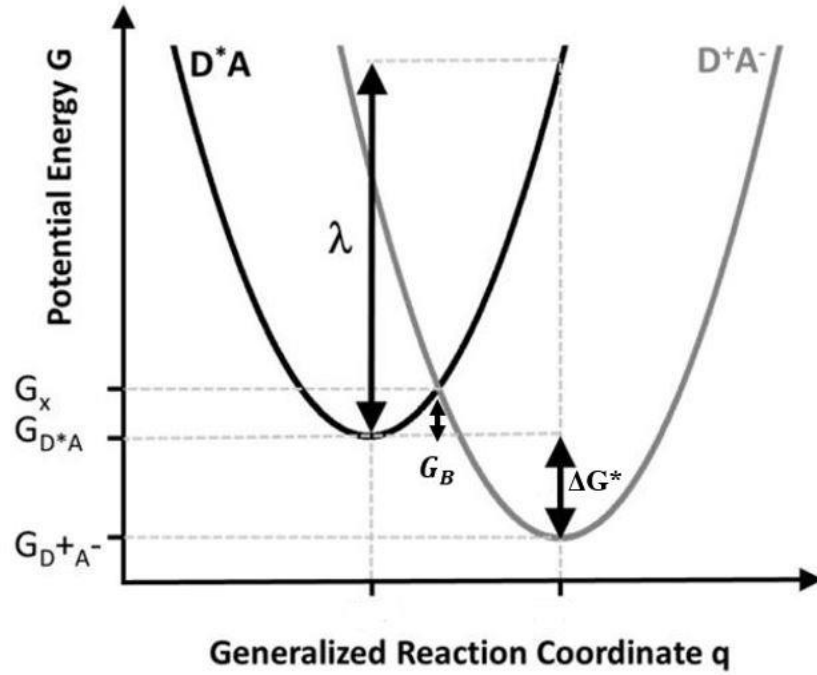


**Figure 23:** Potential energy surfaces of excited ( $D^* A$ ) and charge transfer ( $D^+ A^-$ ) states represented by parabolas.<sup>[23]</sup>

According to Marcus theory, the rate of the electron transfer process is given by:

$$k_{ET} = A \exp \left[ -\frac{G_B}{k_\beta T} \right] = A \exp \left[ -\frac{(\Delta G^* + \lambda)^2}{4\lambda k_\beta T} \right] \quad (9)$$

Where (A) is the coupling constant between donor and acceptor,  $k_\beta$  is Boltzmann's constant at temperature T.<sup>[23]</sup> The rate of electron transfer changes with  $\Delta G^*$ , which can be divided into two regimes: normal regime and inverted regime (Figure 24). In the normal regime  $-\Delta G^* \leq \lambda$ ,  $k_{ET}$  increases with increasing driving force  $-\Delta G^*$ .  $k_{ET}$  is maximized when  $-\Delta G^* = \lambda$  and  $G_B$  disappears in this regime. Moreover,  $k_{ET}$  decreases with increasing the driving force  $-\Delta G^* > \lambda$  and this is called the inverted regime.<sup>[32]</sup>

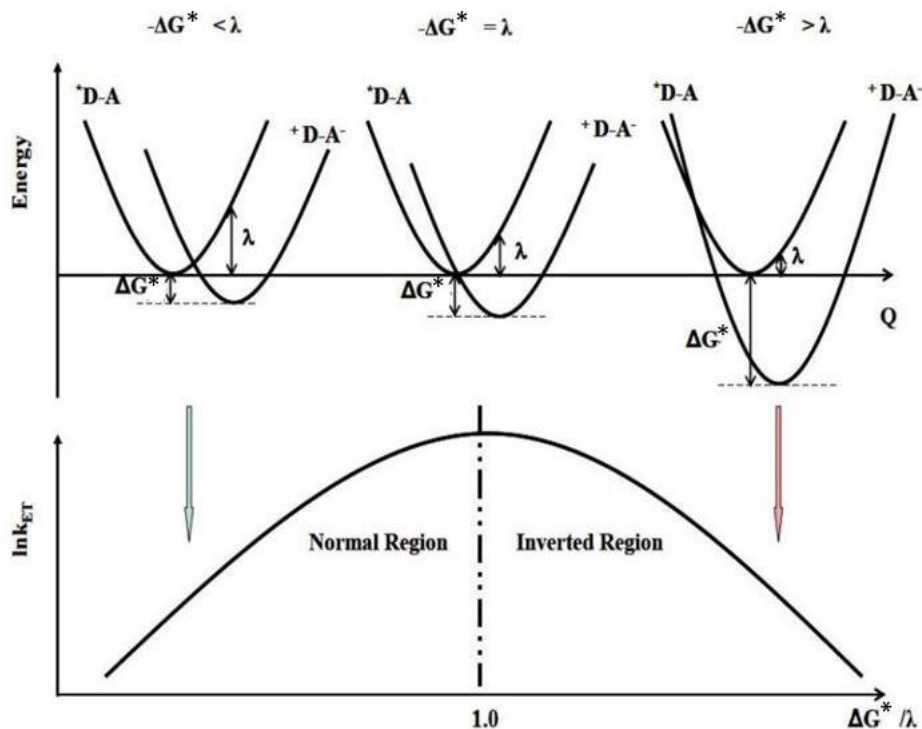


**Figure 24:** Marcus Theory Diagram indicating the normal and inverted regions.<sup>[32]</sup>

Electron transfer decreases when the nuclear positions have to change to reach the crossing point. This requires some energy, because in normal and inverted regimes, the crossing point is not at the bottom of the parabola ( $-\Delta G^* = \lambda$ ). Hence, there is an energy barrier in these regimes.

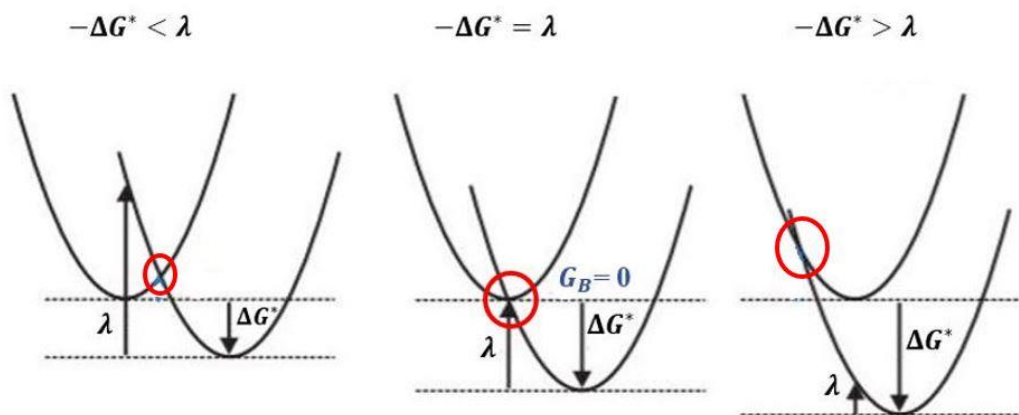


**Figure 25:** The intersection point between the parabolas in different regimes.

The essential goal of this thesis is to study the impact of large IE offsets on IQE, and to reveal whether this relation can be understood by the inverted Marcus regime. Figure 26 shows how increasing the IE offset at the interface between donor and acceptor decreases the  $E_{CT}$ , which is equal to  $G_{D^+A^-}$  in the Marcus model. Consequently, the driving force  $\Delta G^*$  of the exciton to CT-state transition is given by the difference between the free energy of the acceptor exciton  $G_{DA}^*$  approximated by the acceptor's optical bandgap determined at the intersection of the normalized PL and UV-Vis absorption, and CT state energy  $G_{D^+A^-}$ , determined from the difference between the donor's IE and acceptor's EA:

$$\Delta G^* = G_{DA}^* - G_{D^+A^-} \quad (10)$$

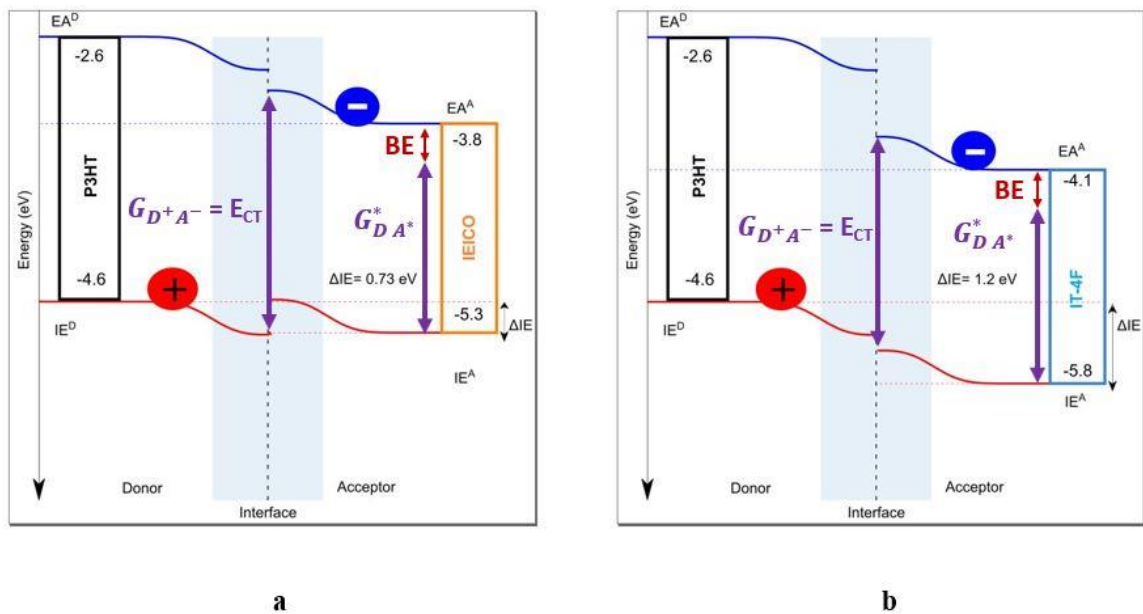


**Figure 26:** IE offsets between a) P3HT:IEICO, b) P3HT:IT-4F. Where,  $G_{DA}^*$  is the optical bandgap of the acceptor, and BE is the binding energy.

## **2.7 P3HT-based organic solar cells**

### **2.7.1 P3HT**

Poly(3-hexylthiophene) P3HT is a widely used polymer in organic electronics due to its simple chemical structure, cost, stability, and scalability. Here, P3HT was used in this work due to its low IE, which results in large IE offsets with many low-bandgap NFAs. Several parameters can change the performance of OSCs, for instance, thermal annealing affects the surface morphology, the quality of the materials used, their dispersity, and regioregularity. The performance of P3HT-based devices is very sensitive to morphology and this often limits the efficiency of P3HT-based OSCs. In general, the photophysical properties of polymers have a significant dependence on their molecular weight.<sup>[35]</sup> Several studies have been conducted to study the molecular weight dependence of P3HT and non-fullerene acceptors in OSCs. Using very high or very low  $M_w$  decreases the power conversion efficiency (PCE).<sup>[35]</sup> Therefore, the  $M_w$  is a critical parameter that has to be carefully controlled to ensure high device performance. (for the  $M_w$  used in this work, see section 3.1.1)

### **2.7.2 P3HT:Fullerene acceptors**

For several decades fullerenes such as PC<sub>60</sub>BM and PC<sub>70</sub>BM remained the only choice as electron acceptors in BHJs based OSCs (figure 27).<sup>[36]</sup> Their unique structure enhances the electron transport and charge separation due to the degeneracy of the LUMO level.<sup>[21]</sup>

Fullerenes can be represented as a cage-like ball structure.<sup>[37]</sup> The wide use of fullerenes in the past was due to their good electron mobility and high electron affinity. However, fullerene acceptors suffer from several issues such as weak solar spectrum absorption because of their chemical and electronic structure, low open-circuit voltage  $V_{OC}$  in devices,

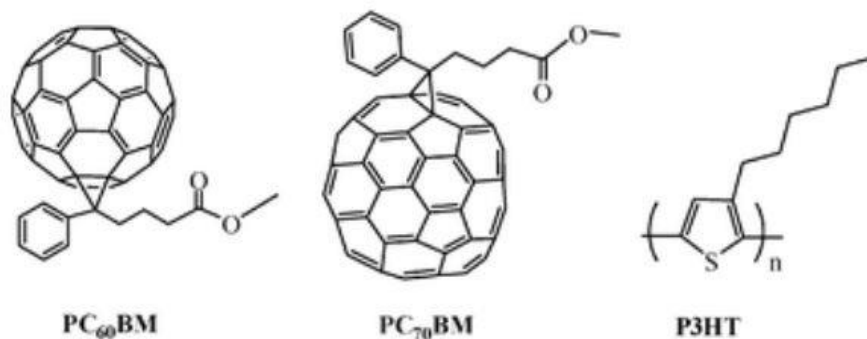


**Figure 27:** (from left to right) The molecular structure of PC60BM, PC70BM, and P3HT.<sup>[38]</sup>

and high synthetic cost.<sup>[36]</sup> Moreover, the highest PCE of P3HT:fullerene-based OSCs is only above 3%, obtained for P3HT:PC<sub>60</sub>BM.

### 2.7.3 P3HT:Non-Fullerene acceptors

Recently, non-fullerene (NFAs) acceptors attracted attention. NFA-based OPVs achieved high PCEs up to 18%, which is much higher than that of any FA-based OSCs.<sup>[40]</sup> The photophysical properties of NFAs-based OPVs enable them to enhance current generation and reduce voltage losses.<sup>[39]</sup> One of the important types of NFAs is rylene diimides (figure 28-a) because of the intermolecular  $\pi$ -stacking. These acceptors provide high electron mobility, thermal stability, and electron affinities.<sup>[40]</sup> Furthermore, fused-ring electron acceptors (FREAs) (figure 28-b) such as IEICO, BT-CIC, and O-IDTBR (figure 29) have

achieved very high PCE due to their physical properties such as broad and strong absorption, high carrier mobility, reduced voltage losses, and high photostability.<sup>[40]</sup> P3HT:NFA-based OSCs have recently achieved 9.5% power conversion efficiency.<sup>[41]</sup>

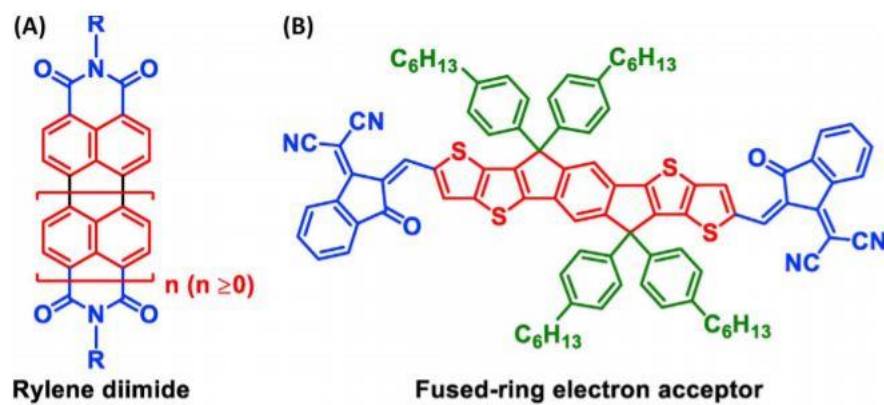


**Figure 28:** Molecular structure of a) Rylene diimide, b) Fused-ring electron acceptor (FREA).<sup>[42]</sup>

## **Chapter 3: Materials and Methods**

### **3.1 Investigated materials**

#### **3.1.1 Donor and acceptor materials**

Different devices were fabricated using an inverted structure. The interlayers of the inverted structure are electron collecting layer (cathode), electron transporting layer (ELT), photoactive layer, hole transporting layer (HTL), and hole collecting layer (Anode) (see figure 32-b). The same donor polymer P3HT was used with six different non-fullerene acceptors (figure 29): BT-CIC, IT-4F, IEICO, IEICO-4F, IEICO-4Cl, and O-IDTBR (for the IUPAC names see page 9). The materials were dissolved in different solvents (CB, DCB, CF, and anisole) and additives (DIO, PN, and CN) were used to optimize the solar cell performance to investigate the effect of the IE offset on the performance of the devices. All the materials used in this work are commercially available. P3HT was purchased from Sigma-Aldrich with  $M_w=17$  kDa. All NFAs were purchased from (1-Material), except O-IDTBR which was purchased from Solarmer. All solvents were purchased from Sigma-Aldrich.

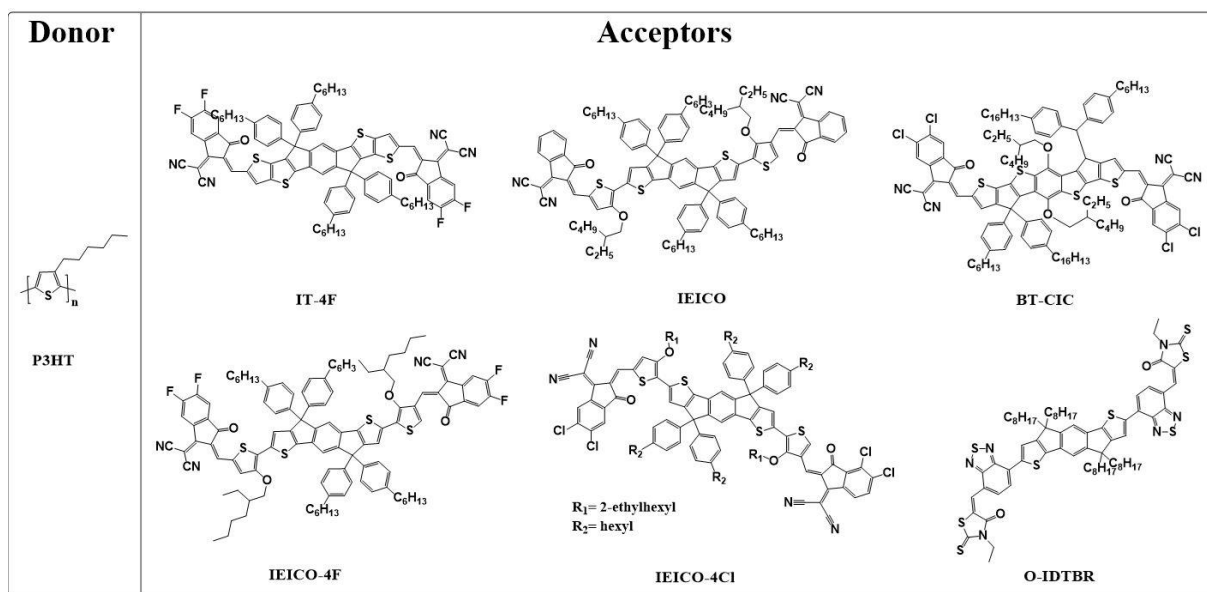


**Figure 29:** Chemical structures of the investigated donor and acceptors materials.

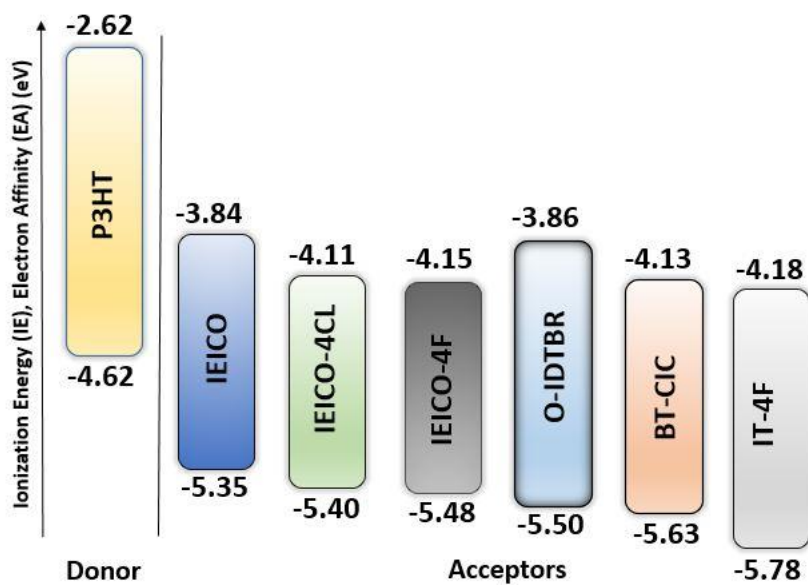


**Figure 30:** Energy levels diagram measured by PESA.

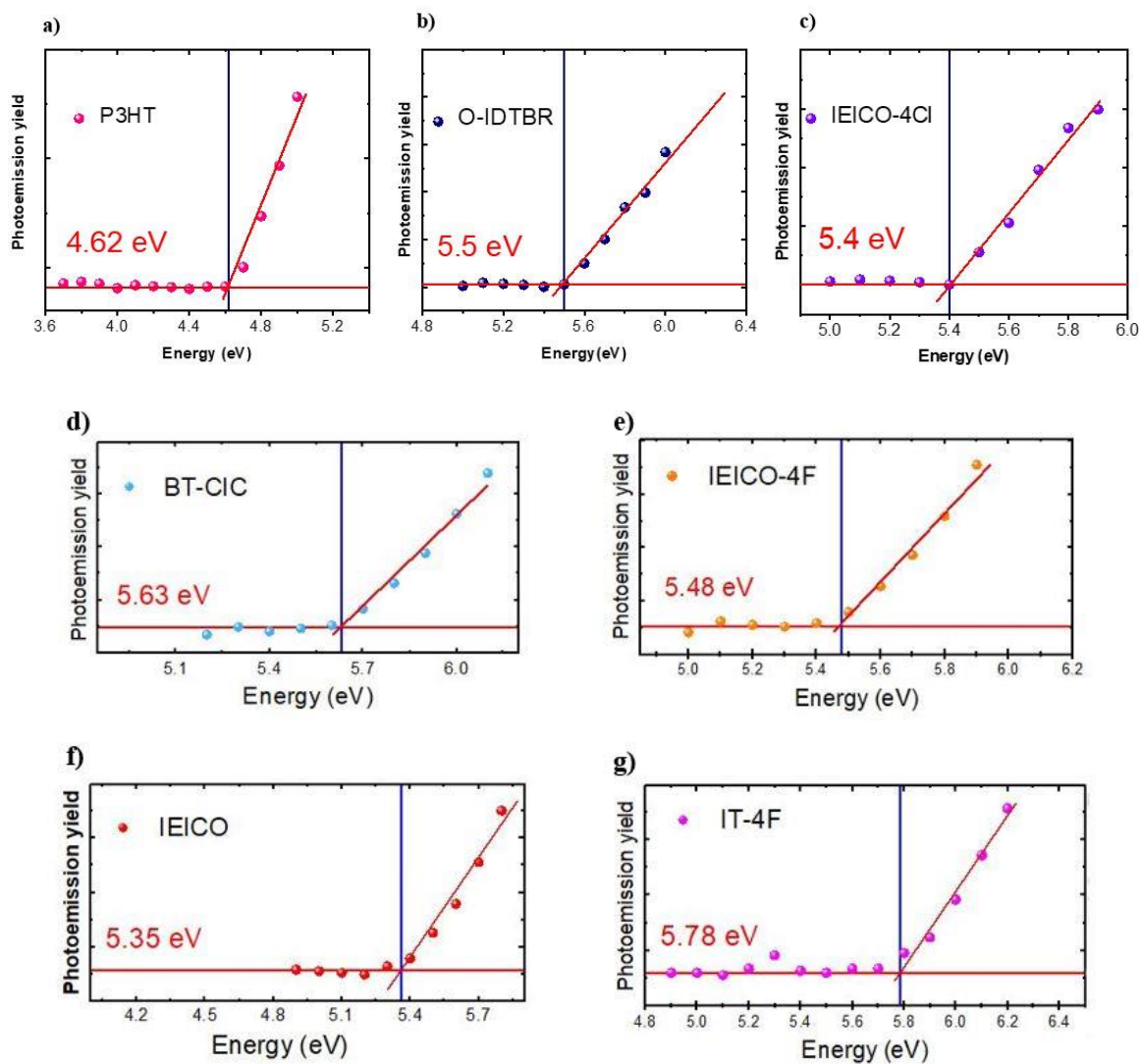


**Figure 31:** IE values using PESA. Figures d, e, f, and g were taken from previous work.<sup>[30]</sup>

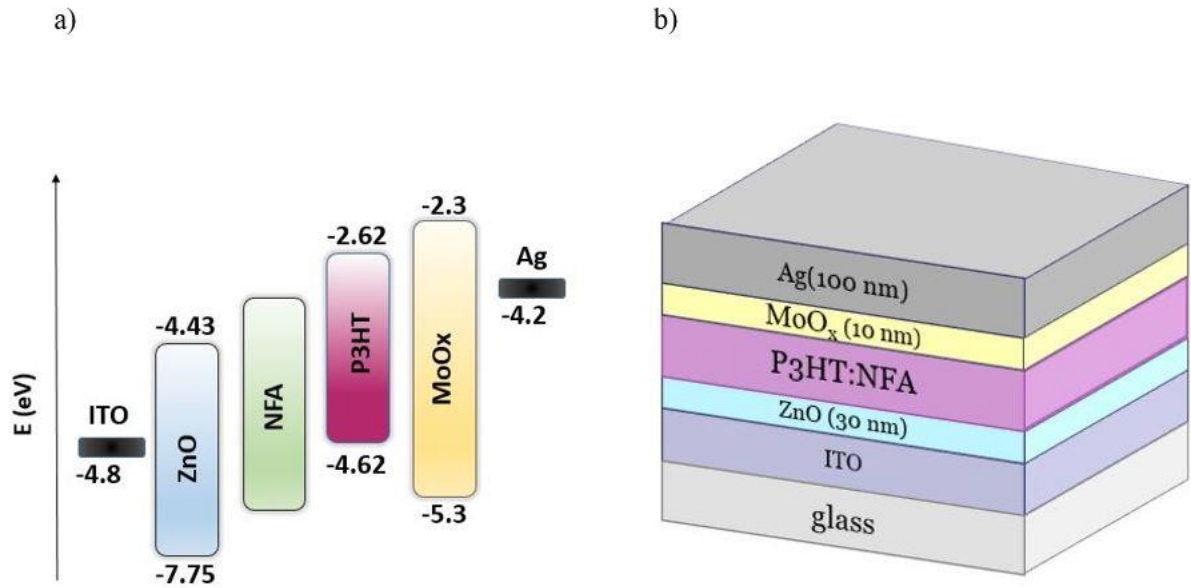


**Figure 32:** a) Energy level diagram of the device (inter)layers. b) Inverted device structure.

### **3.1.2 Device preparation and optimization**

More than 174 devices were fabricated with different conditions to investigate the effect of the IE. All active layer solutions were prepared in a N<sub>2</sub> filled glove box with very low O<sub>2</sub> (below 10 ppm) and H<sub>2</sub>O levels (below 0.1 ppm), then placed on a hot plate at 40°C for CF solutions and 60°C for CB and DCB solutions. 210 rpm was used to stir the solutions for 12 hours. Moreover, spin coating speeds (1000, 1500, 2000, and 2500) rpm and spin coating time 30 seconds were used for each condition in the optimization of the active layer deposition (Tables 1-6).

**Table 1:** Optimization process of P3HT:BT-CIC, shaded area (yellow) represents the best performance.

Active layer	Concentration (mg/mL)	Ratio (D:A)	Solvent	Annealing temperature (°C)	Annealing time (min)
P3HT:BT-CIC	34	1:1	CB	112	10
P3HT:BT-CIC	40	1:1	CB	160	15
P3HT:BT-CIC	20	1:1	CF	160	10
P3HT:BT-CIC	30	2:1	CF	160	10
P3HT:BT-CIC	30	1:2	CF	160	10
P3HT:BT-CIC	30	2:1	CF + DIO (2.5%)	160	15
P3HT:BT-CIC	30	2:1	CF + Anisole (4:6)	160	10
P3HT:BT-CIC	30	2:1	CF + Anisole (8:2)	160	10
P3HT:BT-CIC	30	2:1	CF + Anisole (8:2) + DIO (2.5%)	160	10
P3HT:BT-CIC	30	2:1	CF + PN (2%)	160	10
P3HT:BT-CIC	30	2:1	CF	160	10
P3HT:BT-CIC	20	2:1	CF	160	10

**Table 2:** Optimization process of P3HT:IT-4F, shaded area (yellow) represents the best performance.

Active layer	Concentration (mg/mL)	Ratio (D:A)	Solvent	Annealing temperature (°C)	Annealing time (min)
P3HT:IT-4F	34	1:1	CB	112	10
P3HT:IT-4F	40	1:1	CB	160	15
P3HT:IT-4F	20	1:1	CF	160	10
P3HT:IT-4F	30	2:1	CF	160	10
P3HT:IT-4F	30	1:2	CF	160	10
P3HT:IT-4F	30	1:2	CF + DIO (2.5%)	160	15
P3HT:IT-4F	30	1:2	CF + Anisole (4:6)	160	10
P3HT:IT-4F	30	1:2	CF + Anisole (8:2)	160	10
P3HT:IT-4F	30	1:2	CF + Anisole (8:2) + DIO (2.5%)	160	10
P3HT:IT-4F	30	1:2	CF + PN (2%)	160	10
P3HT:IT-4F	30	1:2	CF + Anisole (8:2) + DIO (2.5%)	160	10
P3HT:IT-4F	20	1:2	CF+Anisole (8:2) + DIO (2.5%) (2.5%)	160	10

**Table 3:** Optimization process of P3HT:IEICO, shaded area (yellow) represents the best performance.

Active layer	Concentration (mg/mL)	Ratio (D:A)	Solvent	Annealing temperature (°C)	Annealing time (min)
P3HT:IEICO	20	1:1	CF	160	10
P3HT:IEICO	20	1:1	CF + DIO (2.5%)	160	10
P3HT:IEICO	20	1:1	CF	160	10
P3HT:IEICO	30	2:1	CF	160	10
P3HT:IEICO	30	1:2	CF	160	10
P3HT:IEICO	20	1:1	CF + DIO (1.5%)	160	15
P3HT:IEICO	20	1:1	CF + Anisole 4:6	160	10
P3HT:IEICO	20	1:1	CF + Anisole 8:2	160	10
P3HT:IEICO	20	1:1	CF + Anisole (8:2) + DIO (2.5%) (2.5%)	160	10
P3HT:IEICO	20	1:1	CF + PN (2%)	160	10
P3HT:IEICO	20	1:1	CB	160	10
P3HT:IEICO	20	1:1	CF	SVA	20

**Table 4:** Optimization process of P3HT:IEICO-4Cl, shaded area (yellow) represents the best performance.

Active layer	Concentration (mg/mL)	Ratio (D:A)	Solvent	Annealing temperature (°C)	Annealing Time (min)
P3HT:IEICO-4CL	20	1:1	CF	160	10
P3HT:IEICO-4CL	20	1:1	CF + Anisole (8:2) + DIO (2.5%)(2.5%)	160	10

**Table 5:** Optimization process of P3HT:IEICO-4F, shaded area (yellow) represents the best performance

Active layer	Concentration (mg/mL)	Ratio (D:A)	Solvent	Annealing temperature (°C)	Annealing Time (min)
P3HT:IEICO-4F	20	1:1	CB	160	10
P3HT:IEICO-4F	20	1:1	CF	160	10

**Table 6:** Optimization process of P3HT:O-IDTBR, shaded area (yellow) represents the best performance

Active layer	Concentration (mg/mL)	Ratio (D:A)	Solvent	Annealing temperature (°C)	Annealing Time (min)
P3HT:O-IDTBR	34	1:1	CB	112	10
P3HT:O-IDTBR	24	1:1	CB	160	15
P3HT:O-IDTBR	25	1:1	DCB	140	10
P3HT:O-IDTBR	30	1:1	CB	140	10
P3HT:O-IDTBR	25	1:1	CF	140	10
P3HT:O-IDTBR	30	1:2	CB	140	10
P3HT:O-IDTBR	24	1:1	CB	140	10

### **3.1.3 Device Layers**

#### **3.1.3.1 Substrates cleaning process**

The first step in device fabrication is cleaning the substrates. Glass substrates with patterned layer of Indium Tin Oxide (ITO) (109 nm) were used (ITO will be discussed in the next section). Substrate cleaning plays an essential role in the overall device efficiency because it is the foundation of all the layers. The substrates should be cleaned from inorganic and organic impurities, which can be done through a multistep process. First, substrates were placed in a Teflon holder and were cleaned with soap and DI water in an ultrasonic bath for 15 minutes. After that, the substrates should get rinsed from any remaining soap, which is very important to ensure smooth solution deposition. Second, Acetone and Isopropanol (IPA) were used successively via ultrasonication for 15 minutes each. Third, substrates were dried using nitrogen gas. Finally, substrates were placed in plasma treatment for 20 minutes to clean the organic impurities and adjust the work function of the ITO.

#### **3.1.3.2 Electron collecting electrode**

Transparent glass with a patterned layer of ITO substrates were used as a base for all the layers deposition. The size of the glass substrate that covered by ITO patterns is 25.4x25.4x1.1 mm (figure 33). ITO is commonly used in device fabrication due to its transparency, stability, and good adhesion of the next layer. Devices were fabricated using an inverted structure. Therefore ITO works as an electron collecting layer (Cathode).

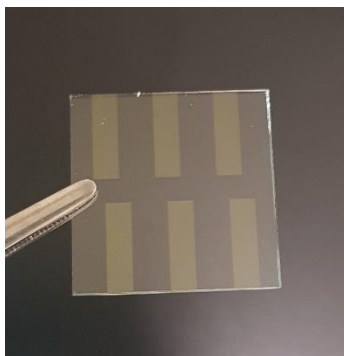


**Figure 33:** ITO substrate.

### **3.1.3.3 Electron transporting layer**

On top of the ITO a thin layer of ZnO was deposited to form an approximately 30 nm thick layer. ZnO was prepared in the laboratory by dissolving Zn(OAc)<sub>2</sub> in monoethanolamine (60 $\mu$ L) and 2-methoxyethanol (2 mL). 60  $\mu$ L of ZnO solution was spin coated at 4000 rpm for 30 seconds, after that, the edges of the ITO were cleaned from the ZnO using DI water to have an accessible contact to the electrode (ITO). Next, films were baked at 150 °C for 10 minutes. ZnO acts as electron transporting layer, therefore, this layer enhances the electrons diffusion and blocks the extraction of the holes from the active layer.

### **3.1.3.4 Active layer**

Active layers solutions were deposited inside N<sub>2</sub> filled glovebox using spin-coater purchased from Specialty Coating System (Model G3P-8) with different rpm (as discussed earlier). The photoactive layer deposition is followed by removing part of the active layer from the edges of the ITO, this can be done by solvents or using blades. Next, all the films were placed on a hot plate for thermal annealing at different temperatures and different

annealing times. Thermal annealing changes the morphology of the active layer, therefore, enhances the distribution between donor and acceptor materials. The active area of all the devices used is  $0.1 \text{ cm}^2$ .

### 3.1.3.5 Hole transporting layer

A very thin layer of Molybdenum Oxide ( $\text{MoO}_x$ ) was thermally evaporated through a shadow mask with a deposition rate  $10 \text{ \AA/s}$  (at a pressure less than  $2 \times 10^{-6} \text{ Torr}$ ) and deposited onto the active layer equal to  $10 \text{ nm}$ . In contrast to the ETL) the HTL enhances the extraction of holes and acts as electron blocking layer.  $\text{MoO}_x$  was chosen for its high transparency and stability.

### 3.1.3.6 Hole collecting layer

Silver (Ag) with  $100 \text{ nm}$  thickness was thermally evaporated on the  $\text{MoO}_x$ , and that was the last layer in the device which is hole collecting layer (Anode). Ag was chosen due to its high work function, stability, and conductivity.  $\text{ITO}/\text{ZnO}/\text{P3HT:NFA}/\text{MoO}_x/\text{Ag}$  is the final structure for all the devices used in this work.

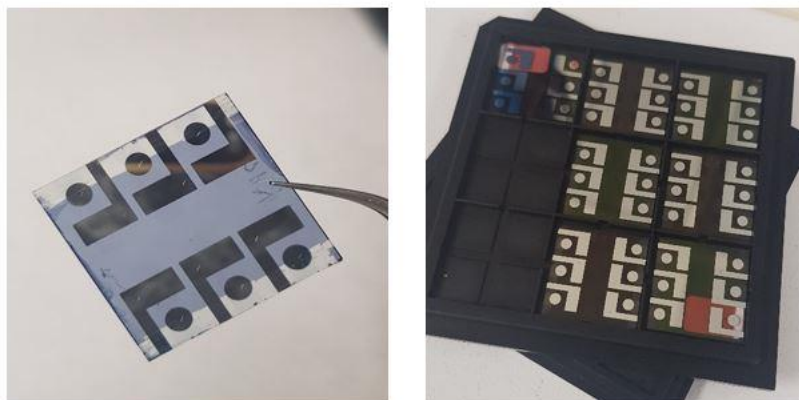


**Figure 34:** Final structure of OSCs.

## **3.2 Device Characterization Techniques**

### **3.2.1 J-V Characterization**

The fabricated devices were illuminated in N<sub>2</sub> filled glovebox using a solar simulator to extract the current density-voltage characteristics (J-V curve). Oriel Sol3A class AAA solar simulator was used with a Keithley 2400 source meter to measure the J-V curves of the devices. The solar simulator is set to 1 Sun (1000 W/m<sup>2</sup>) and calibrated so that the spectrum is compliant with AM1.5G. The software provides figures of merit, V<sub>OC</sub>, J<sub>SC</sub>, FF, and PCE.

### **3.2.2 External Quantum Efficiency (EQE)**

The external quantum efficiency (EQE) characteristics were obtained at zero bias by illuminating the active area of the device with individual wavelengths selected using a monochromator from a Xenon arc lamp broad spectrum light source . A silicon photodiode calibrated by NIST was used to calculate the number of incident photons at each wavelength from 300 nm to 1100 nm. The current was measured to calculate the number of electrons extracted from the device.

## **3.3 UV-Vis Spectrophotometry**

Absorbance and transmission spectra of the active blend films on quartz substrates were measured using a UV-VIS absorption spectrometer (Cary 5000) calibrated for Baseline (0%) and 100% transmittance. The wavelengths used to measure the absorbance for P3HT were (200 - 800nm) and for NFAs (200 nm - 1200 nm).

### **3.4 Photoluminescence Spectroscopy**

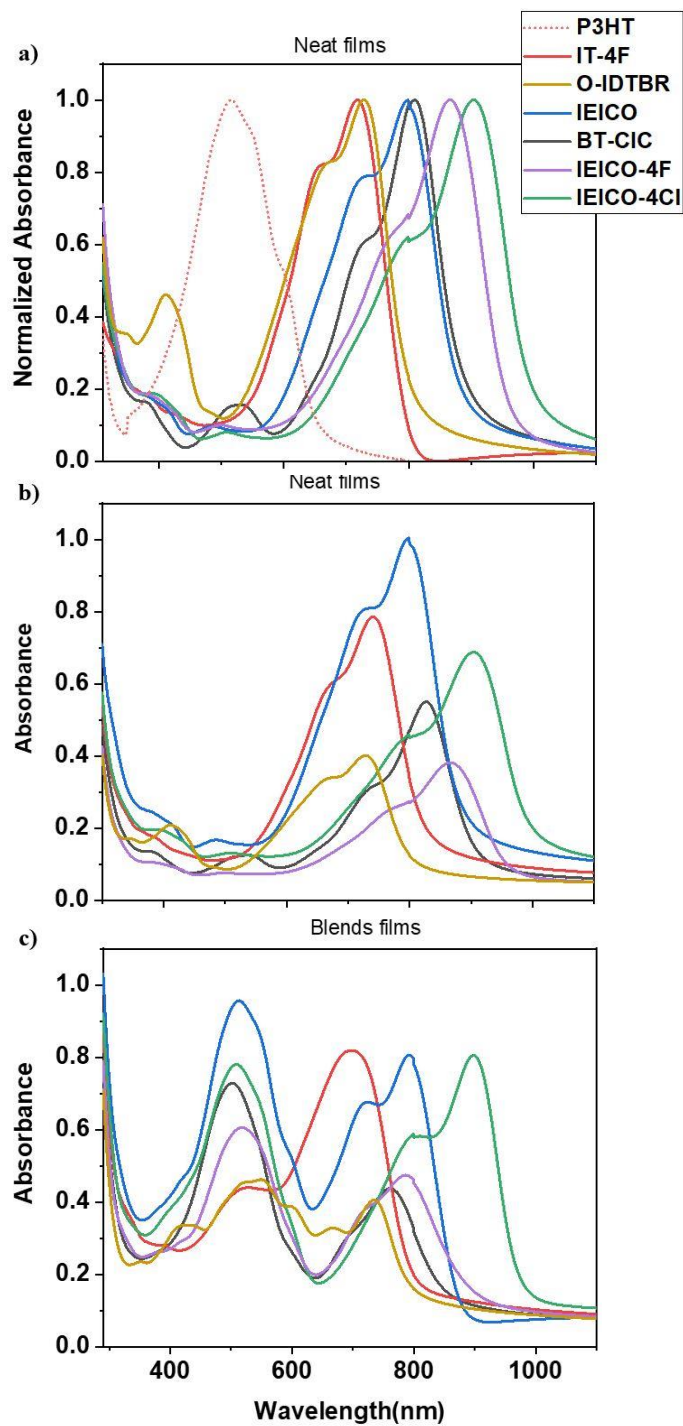
To measure the fluorescence of the active layers, Horiba FluoroMax PL spectrometer was used. Different excitation wavelengths, slit size and wavelength range were used depending on the absorption spectra of each sample.

### **3.5 Profilometer**

A Profilometer was used to measure the thicknesses of the active layers. Tensor stylus profiler (Tensor P-6) has a probing tip that works under a force equal to 0.5 mN. The films were scratched and placed on a moving stage to calculate the thickness variations across the scratch.

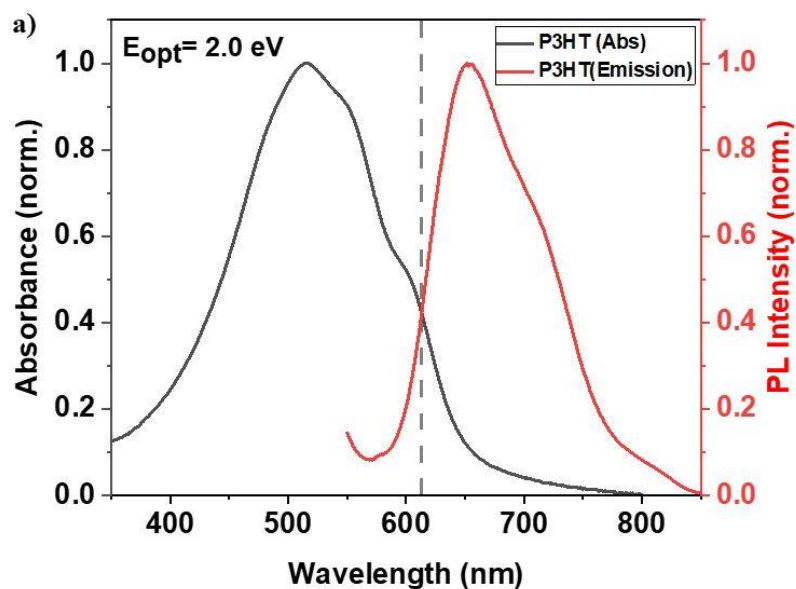
## Chapter 4: Results and Discussion

### 4.1 UV-vis Absorption and Photoluminescence (PL) / Optical bandgaps



**Figure 35:** UV-vis absorption (absorbance) spectra of a) neat films, b) neat films (non-normalized), c) donor-acceptor blend films.

Figure (35-a) displays the normalized absorption spectra of the donor P3HT and the six NFAs, where P3HT has an absorption range of 300 - 600nm. Since the neat film absorption of O-IDTBR, IT-4F, and IEICO partially overlaps with P3HT, their blend films should exhibit a higher extinction coefficient in the wavelength range 500-600nm. Further red-shifted UV-vis absorption spectra and smaller bandgaps are observed in BT-CIC, IEICO-4Cl, and IEICO-4F. Figure (35-b) shows the measured (non-normalized) absorbance of the neat films. Here, IEICO exhibits the highest absorbance due to its thickness (the thickness of the films is discussed below (section 4.2)). Figure (35-c) shows the absorbance spectra of the blends. Here, P3HT:IEICO-4Cl is the most red-shifted blend due to the low bandgap of the acceptor. All blends exhibit two peaks, the first one around 500 nm where the donor absorption peaks and the second one, where the acceptor absorption peaks.



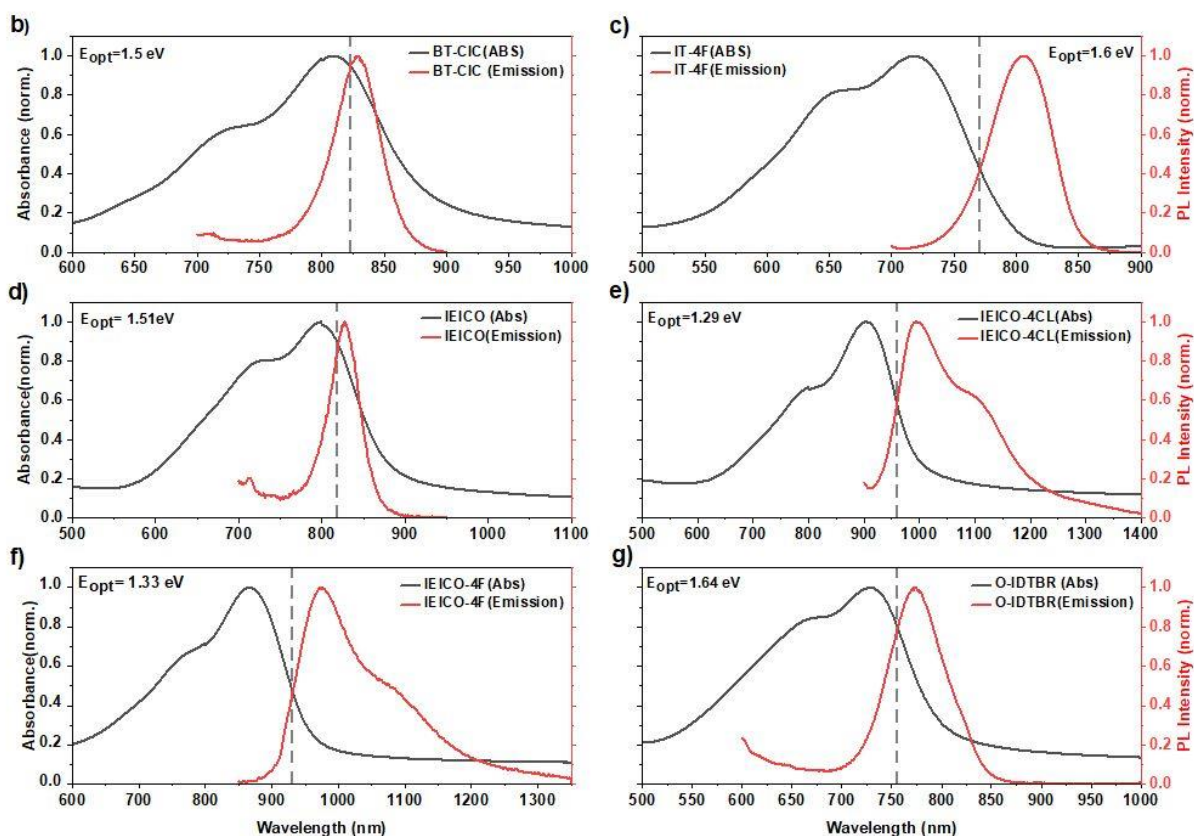


**Figure 36:** Normalized absorbance and emission spectra and optical bandgaps indicated by the dashed vertical lines of a) P3HT, b) BT-CIC, c) IT-4F, d) IEICO, e) IEICO-4Cl, f) IEICO-4F, and g) O-IDTBR.

The intersection between the absorbance spectrum from UV-Vis spectrophotometry and the photoluminescence emission spectrum measured by PL spectroscopy is taken as the optical bandgap. We use the optical bandgaps,  $E_{opt}$ , as an approximate measure of the electron affinity ( $\sim$ LUMO) of the donor and the acceptors, as  $IE - E_{opt}$ . The IE ( $\sim$ HOMO) was measured by PESA for all the materials shown above.

In contrast to the NFAs used in this work, the photoluminescence of P3HT is in the visible range that means smaller wavelength and larger energy. Due to the red-shifted absorption and emission of IEICO-4Cl, it has the smallest  $E_{opt}$ .

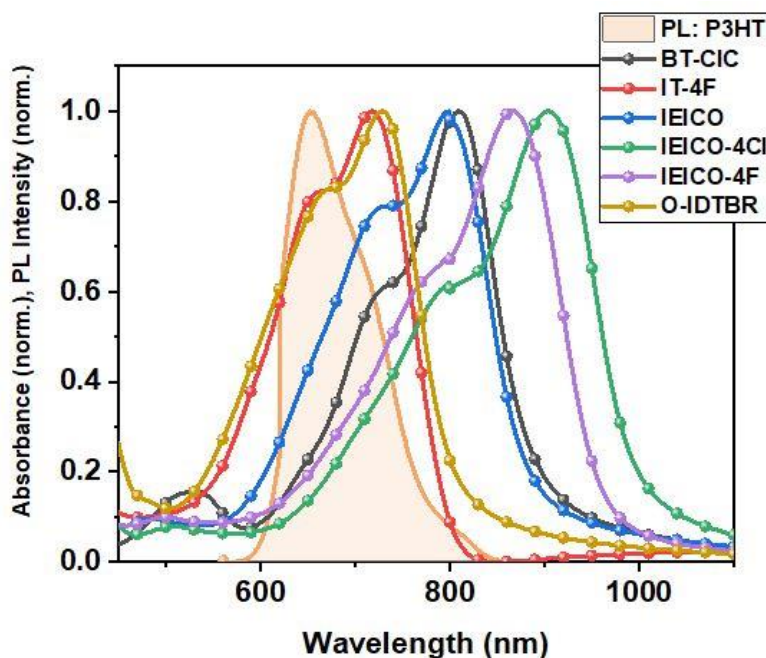


**Figure 37:** Overlap of donor PL (normalized) and acceptor absorbance spectra indicating the possibility of energy transfer from the donor to the acceptors.

Figure 37 shows the spectral overlap between the photoluminescence of the donor P3HT and the absorbance spectra of the NFAs. It indicates that Förster resonance energy transfer (FRET) is very likely to happen. Upon donor excitation, the exciton can be transferred to the acceptor. This explains why holes are transferred from the acceptor to the donor before electrons can transfer from the donor to the acceptor. Consequently, hole transfer is directly related to IE offsets, which is the main subject of this study.

## 4.2 J-V Characteristics

In this thesis, the focus is on charge generation, especially the charge transfer efficiency, estimated by the devices photocurrent at short circuit,  $J_{SC}$ . Therefore,  $V_{OC}$  and FF are not further discussed in detail in this work, they are subject of ongoing and future works. However,  $V_{OC}$  is expected to be low due to the small (diagonal) gap between the HOMO of the donor and the LUMO of the acceptor (figure 30). Here, the systems were used to achieve large IE offsets between donor and acceptor to study the influence of very large IE offsets on charge generation and device efficiency.

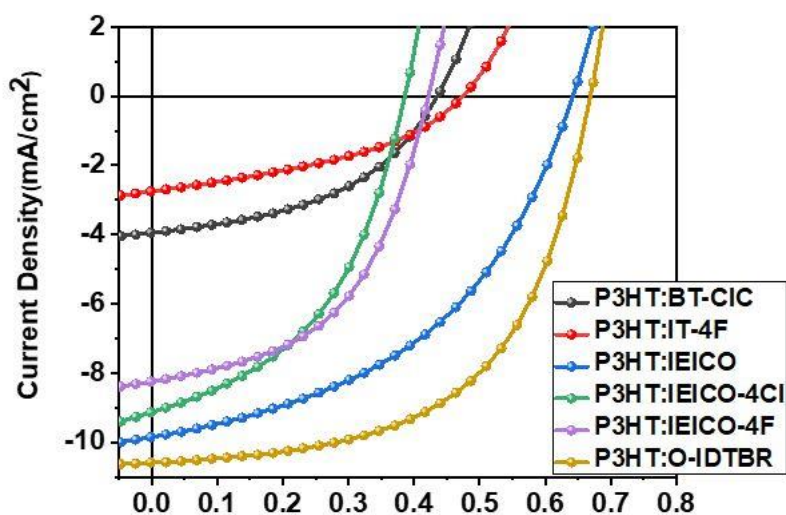


**Figure 38:** J-V curves of the best performance of P3HT:NFA based OSCs.

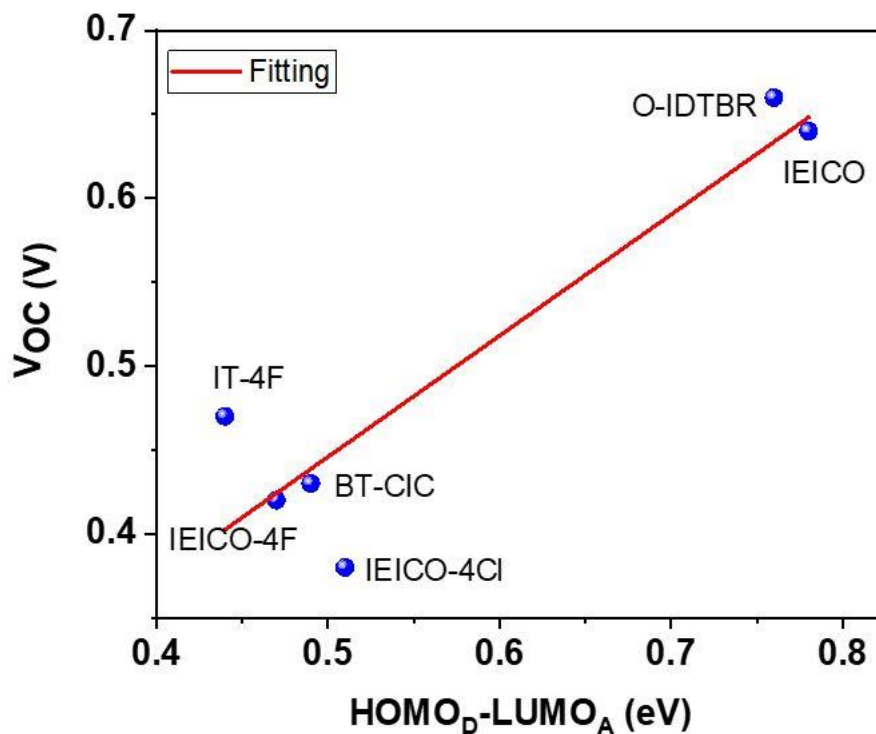
Figure 38 shows the J-V curves of the best devices that were obtained in this work. Over 170 devices were fabricated with an inverted structure: ITO/ZnO/P3HT:NFA/MoO<sub>x</sub>/Ag using different active layer preparation conditions (see section 3.1.2). The J-V curves show that O-IDTBR achieved the highest  $J_{SC}$  therefore, the highest PCE. On the other hand, IT-4F exhibited the lowest  $J_{SC}$  and PCE, and this may be related to the large IE offset between P3HT and IT-4F. Table 7 provides all device figures of merit.

**Table 7:** Figures of merit of P3HT:NFA OSCs in order of decreasing IE offset.

<b>Device</b>	<b><math>\Delta</math> IE (eV)</b>	<b>Thickness (nm)</b>	<b><math>V_{oc}</math> (V)</b>	<b><math>J_{sc}</math> (mA/cm<sup>2</sup>)</b>	<b>FF (%)</b>	<b>PCE (%)</b>
P3HT:IT-4F	1.16	93	0.47	2.75	39.99	0.52
P3HT:BT-CIC	1.01	113	0.43	3.94	45.53	0.78
P3HT:O-IDTBR	0.88	80	0.66	10.57	56.57	4.00
P3HT:IEICO	0.86	196	0.64	9.85	45.43	2.87
P3HT:IECO-4Cl	0.78	156	0.38	9.13	45.55	1.61
P3HT:IEICO-4F	0.73	104	0.42	8.24	50.02	1.74

Moreover, the thickness of the photoactive layer plays an important role in both photon absorption and charge extraction. Thick active layers absorb more photons, but this enhances the charge recombination therefore, less free charges can be extracted from the device. We used very thin photoactive layers of P3HT:O-IDTBR (80 nm), because with increased thickness of P3HT:O-IDTBR, a lot of recombination occurred and therefore the PCE was lower. However, lower thickness reduces the absorption of the photoactive layer (figure 35-b). P3HT:IEICO and P3HT:IEICO-4Cl used thicker photoactive layers equal to

196 nm and 156 nm, respectively, and these blends achieved higher performance with thicker films compared to P3HT:O-IDTBR.



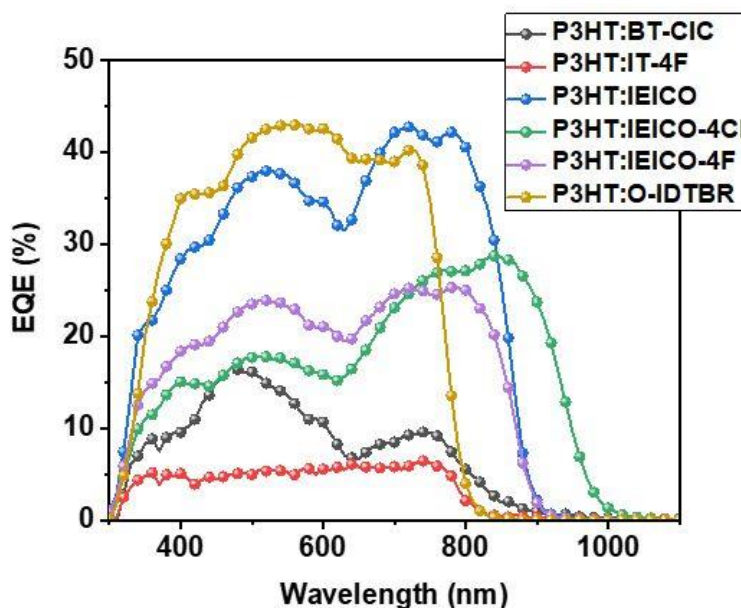
**Figure 39:** Relation between the  $V_{OC}$  and the optical bandgap between the HOMO of the donor and the LUMO of the acceptor.

Figure 39 illustrates the relation of the  $V_{OC}$  of the systems used here and the bandgap between the HOMO of the donor and the LUMO of the acceptor. Although the LUMO levels are not the exact values, they still provide qualitative insight. Increasing the (diagonal) bandgap increases the  $V_{OC}$  however, most of the systems used have very small bandgaps due to the large IE offsets between donor and acceptor.

The fill factor FF of all systems is very low, except for P3HT:O-IDTBR, which also has high  $V_{OC}$ . The low FF indicates that there is another effect either in the charge generation process (competing with geminate recombination) or in the charge extraction (competing with non-geminate recombination).

### 4.3 External Quantum Efficiency (EQE)

$J_{SC}$  is not sufficient to investigate the charge transfer, because some blends have much broader absorption than others. The EQE gives provides information about the number of charges extracted from the device per incident photons.



**Figure 40:** External quantum efficiency (EQE) spectrum of P3HT:NFA OSCs.

Figure 40 shows the EQE of the six systems investigated in this thesis. All the systems exhibit low EQE values of less than 45% as expected from the low photocurrent that can be extracted from these devices. P3HT:O-IDTBR has the best performance among all

systems with 4% PCE and  $J_{SC} = 10.57 \text{ mA/cm}^2$ . Due to the high EQE of 42% at 560 nm, the system delivers high  $J_{SC}$  compared to the other systems. In contrast to P3HT:O-IDTBR, P3HT:IT-4F exhibits the lowest device performance with less than 1% PCE and an EQE of 6% at 640 nm, and a FF of 40%. P3HT:IEICO, P3HT:IEICO-4Cl, and P3HT:IEICO-4F are red shifted due to their smaller bandgaps, and they have stronger peaks in the NIR region, which is the absorption region of the acceptors unlike the visible region, where the absorption of the donor occurs. The EQE of P3HT:BT-CIC peaked at 480 nm with 16% corresponding to the blend absorption spectra.

### 4.3 Internal Quantum Efficiency (IQE)

The EQE provides a better comparison than the  $J_{SC}$ , since we are interested in the charge generation efficiency concerning the Marcus theory. However, the IQE is an even better measure. It is defined as the number of electrons out per number of photons absorbed.

The IQE calculation was done by considering the reflectance and the parasitic absorption of the device stack, that is the absorption that does not lead to exciton generation and competes with excitation of the photoactive layer in turn reducing the photocurrent of the devices. The IQE was calculated by the following equation<sup>[43]</sup>

$$IQE = \frac{EQE}{1 - R\% - \text{Parasitic absorption}} \quad (11)$$

Where the parasitic absorption and the reflectance of each layer of the device were obtained by transfer matrix simulation (figure 41).

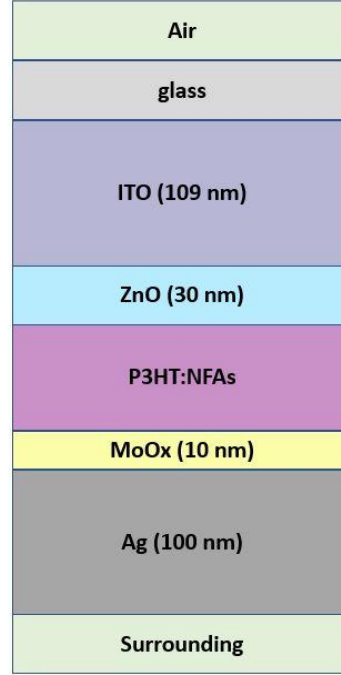


**Figure 41:** Simulated device structure.

First, the wavelength-dependent absorption coefficient  $\alpha(\lambda)$  of the photoactive layers was calculated from the absorbance using the following expression:

$$\alpha(\lambda) = \frac{\ln(10) \times A}{d} \quad (12)$$

Where (A) is the absorbance from the UV-vis spectra, and (d) is the film thickness (nm).

From equation (12), the extinction coefficient  $k(\lambda)$  was calculated using equation (13).

$$k(\lambda) = \frac{\alpha(\lambda) \times \lambda}{4\pi} \quad (13)$$

All the refractive indexes of the layers except the photoactive layer were measured and reported in previous works.<sup>[43]</sup> The real part of the optical constant  $n(\lambda_i)$  was estimated from the imaginary part of the optical constant  $k(\lambda)$  using Kramers-Kronig relation:

$$n(\lambda_i) = \frac{2}{\pi} \mathcal{P} \int_0^{\infty} \frac{\lambda k(\lambda) d\lambda}{\lambda^2 - \lambda_i^2} \quad (14)$$

Where  $\mathcal{P}$  is the Cauchy principal value.

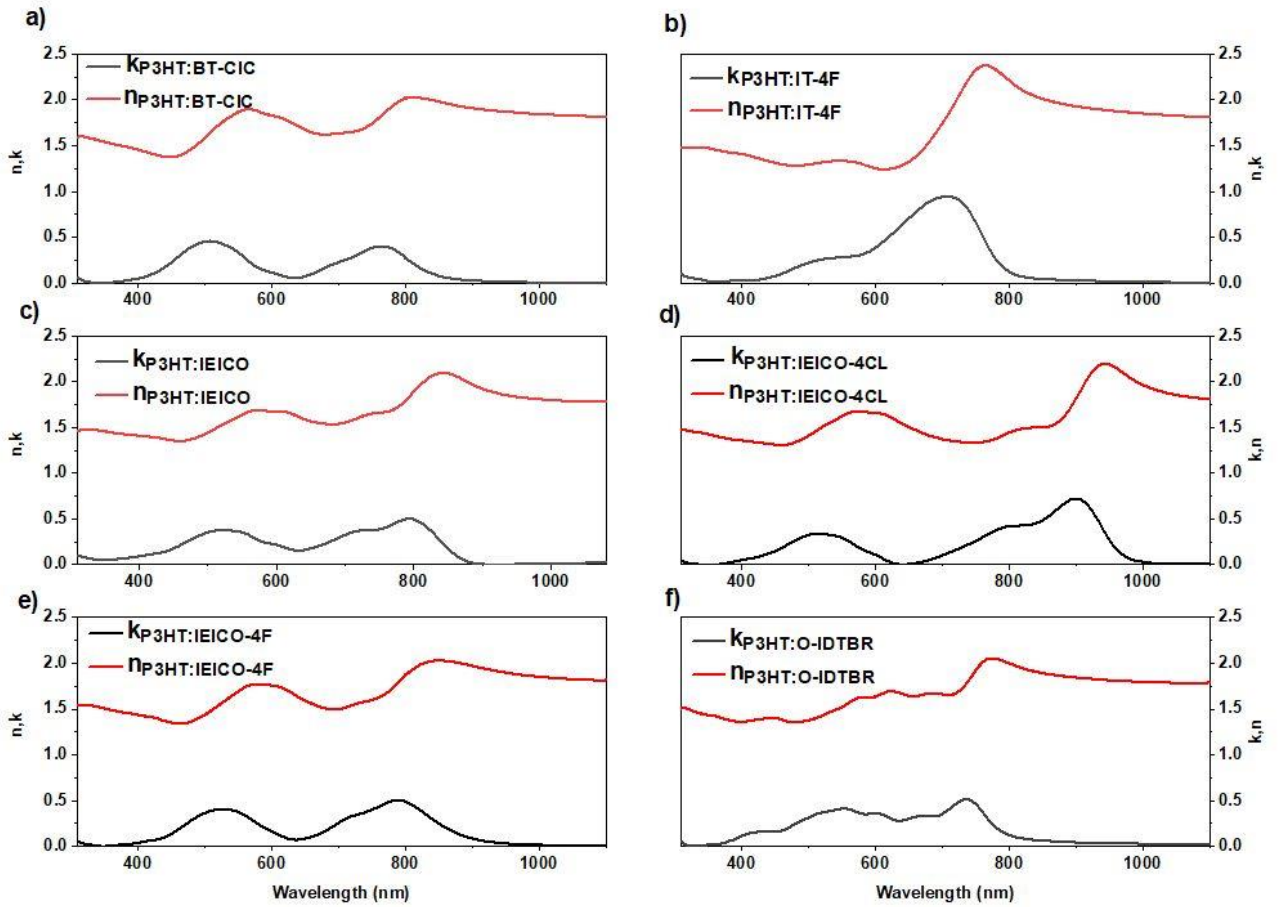


**Figure 42:** Extinction coefficients  $k$  and refractive indexes  $n$  of the active layers of a) P3HT:BT-CIC, b) P3HT:IT-4F, c) P3HT:IEICO, d) P3HT:IEICO-4CL, e) P3HT:IEICO-4F, f) P3HT:O-IDTBR.

Figure 42 displays the spectra of both imaginary and real parts of the optical constant. However,  $n(\lambda_i)$  values were shifted so that the longest wavelength was equal to the square root of a typical organic semiconductor dielectric constant of  $\varepsilon_i = [n(\lambda = \infty)]^2 = 3.3$ . This shift was necessary to compensate for the missing part of the integral as  $k(\lambda)$  is only known for a part of the spectra. Kramers-Kronig relation yields a very good approximation that can be compared to real measurements.<sup>[43]</sup>

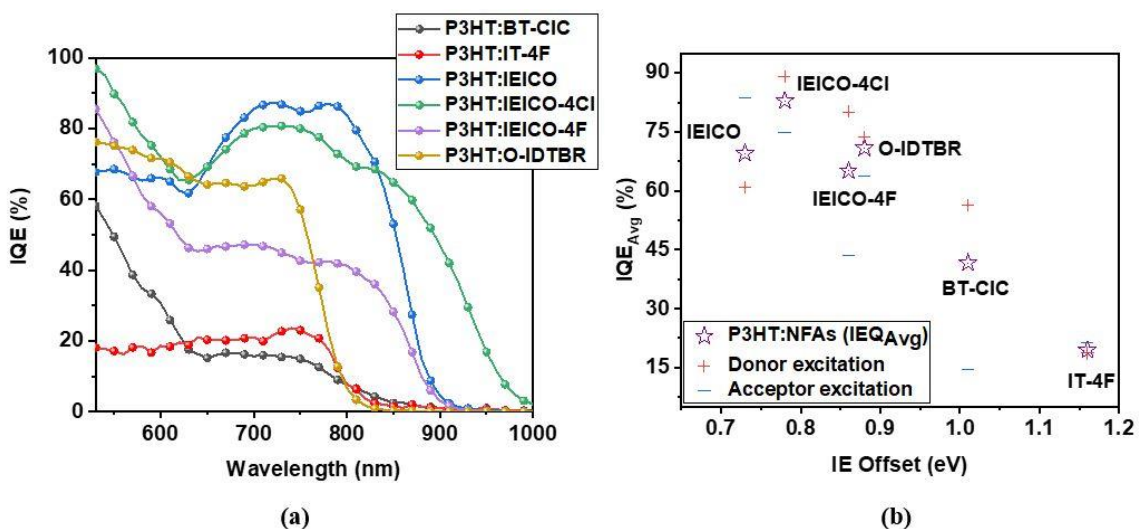


**Figure 43:** a) Internal quantum efficiency (IQE) of P3HT:NFA OSCs, b) averaged IQE vs. IE offsets.

The IQE was calculated using equation (11). Figure (43-a) displays the IQE of all systems used, showing two different regions. In most of the systems, the region where the donor absorbs exhibits a higher IQE than the region where the acceptor absorbs. The IQE appears to diverge in the UV region, potentially because the absorbance was not sufficient in this spectral region to get reliable  $n$  indexes when using equation (14), so the UV part was disregarded. P3HT:BT-CIC and P3HT:IT-4F have low IQE values compared to the other systems, and this can be related to their very large IE offsets (figure 30) with P3HT. The

IQE decreases with increasing the IE offset, which may indicate that the systems chosen reach the Marcus-inverted regime (see chapter 2.6.3). The electron transfer rate (and thus efficiency) decreases with increasing the energy offsets between donor and acceptor, limiting the exciton to charge conversion.

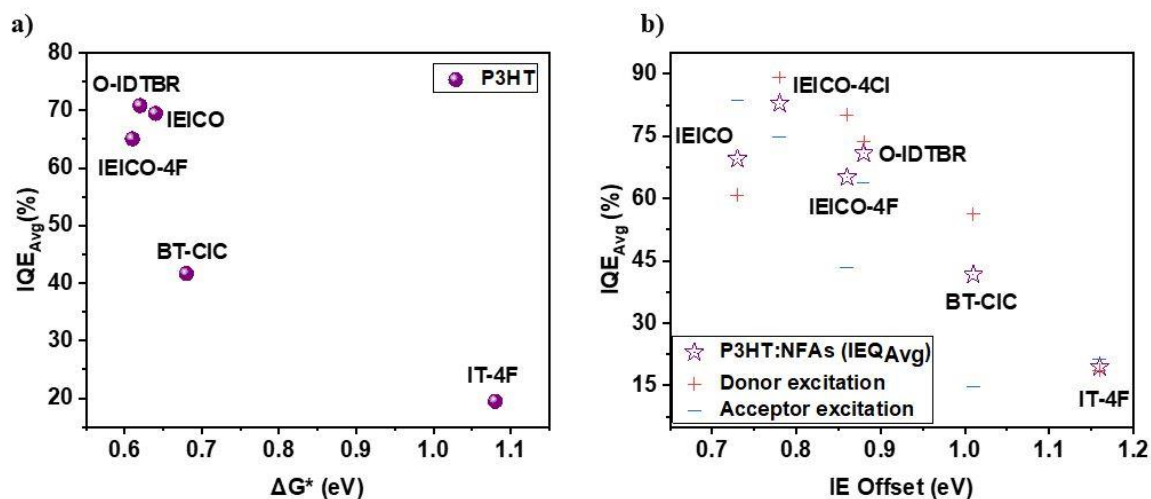


**Figure 44:** Dependence of IQE on a) driving force  $\Delta G^*$  and b) IE offset.

Figure 44a,b illustrate the dependence of the IQE on the driving force  $\Delta G^*$  and the IE offset between donor and acceptor. Using equation (10) allowed to estimate  $\Delta G^*$  as discussed in (2.6.3). Here, we used the EA values from our previous work to calculate approximate CT state energies.<sup>[30]</sup> This estimation provides approximate  $\Delta G^*$  values (figure 44-a) compared to the precise IE offsets determined in this work (figure 44-b). The observed dependence implies that the Marcus-inverted regime is reached for very large IE offsets.

## **Chapter 5: Conclusion and Future Work**

### **5.1 Conclusion**

This study provides insight into the photophysics of donor:NFA systems with large IE offsets between the electron donor polymer P3HT and the non-fullerene electron acceptor. The main subject of the study was to investigate the effect of very large IE offsets on the IQE in the framework of Marcus theory. This finding gives us a better understanding of the charge transfer process between the donor and acceptor. In fact, the study did not aim to achieve high device performance, since large IE offsets were expected to limit the Voc, and this study confirms this. The PCE ranged from 0.5%- 4%, which is low compared to recent state-of-the-art OPVs.

It appears the IE plays an essential role in both charge generation and CT state exciton dissociation. Our results provide evidence that large IE offsets negatively impact the IQE, more precisely the charge transfer process between the donor and acceptor. However, further studies are required to investigate the reasons behind this low charge transfer efficiency (see 5.2) and to exclude other reasons for the lower performance.

In conclusion, there seems to be an optimum range of IE offsets for device performance, and both too low and very high offsets seem to impede efficient charge generation.

## **5.2 Future work**

Several other reasons could also explain the lower IQE that was observed in this work including exciton quenching, charge recombination and limited extraction, in part caused by different sample morphologies. These reasons can be investigated using other spectroscopic techniques:

### **5.2.1 Exciton Quenching / Charge Transfer**

Time-resolved photoluminescence (TR-PL) spectroscopy will be used to measure the lifetime of the photogenerated excitons thereby studying the exciton quenching and charge transfer dynamics. TR-PL will be very important to understand the dynamics of exciton quenching and charge transfer in these systems.

### **5.2.2 Charge Recombination**

Transient Absorption (TA) a pump-probe spectroscopy technique will be used to measure the absorption of excited states and their lifetimes.<sup>[44]</sup> This will be very helpful to investigate the type of charge recombination processes that take place in the systems used in this work.

### **5.2.3 Morphology Studies**

Transmission Electron Microscopy (TEM) will be used to obtain an image of the photoactive layer showing how the donor and acceptor are mixed. This can help to understand the morphology of the blends, specifically the intermixing of donor and acceptor materials.

**BIBLIOGRAPHY**

1. Lopez, Anthony, Billy Roberts, Donna Heimiller, Nate Blair, and Gian Porro. US Renewable Energy Technical Potentials. A GIS-Based Analysis. No. NREL/TP-6A20-51946. National Renewable Energy Lab.(NREL), Golden, CO (United States), 2012.
2. Abdelkareem, Mohammad Ali, M. El Haj Assad, Enas Taha Sayed, and Bassel Soudan. "Recent progress in the use of renewable energy sources to power water desalination plants." *Desalination* 435 (2018): 97-113.
3. Mohtasham, Javid. "renewable energies." *Energy Procedia* 74 (2015): 1289-1297.
4. "U.S. Renewable Energy Factsheet." U.S. Renewable Energy Factsheet | Center for Sustainable Systems. [Online] Available at: <http://css.umich.edu/factsheets/us-renewable-energy-factsheet>.
5. "History of Solar Energy: Who Invented Solar Panels?" History of Solar Energy: Who Invented Solar Panels? | Vivint Solar Learning Center. [Online] Available at: <https://www.vivintsolar.com/learning-center/history-of-solar-energy>.
6. Xiao, Weidong, William G. Dunford, and Antoine Capel. "A novel modeling method for photovoltaic cells." In 2004 IEEE 35th Annual Power Electronics Specialists Conference (IEEE Cat. No. 04CH37551), vol. 3, pp. 1950-1956. IEEE, 2004.

7. "Best Research-Cell Efficiency Chart." NREL.gov. Accessed June 23, 2021.  
[Online] Available at: <https://www.nrel.gov/pv/cell-efficiency.html>.
8. "Solar Radiation Basics." Energy.gov. [Online] Available at:  
<https://www.energy.gov/eere/solar/solar-radiation-basics#:~:text=Solar%20radiation%2C%20often%20called%20the,using%20a%20variety%20of%20technologies>.
9. "Solar Irradiance." Wikipedia. Wikimedia Foundation, April 14, 2021. [Online]  
Available at: [https://en.wikipedia.org/wiki/Solar\\_irradiance](https://en.wikipedia.org/wiki/Solar_irradiance).
10. Hakim, Greg. Department of Atmospheric Sciences. [Online] Available at:  
<https://atmos.washington.edu/~hakim/101/radiation/>.
11. Zhang, Jingjiao, Xiaodong Su, Mingrong Shen, Zhihua Dai, Lingjun Zhang, Xiyun He, Wenxiu Cheng, Mengyu Cao, and Guifu Zou. "Enlarging photovoltaic effect: combination of classic photoelectric and ferroelectric photovoltaic effects." *Scientific reports* 3, no. 1 (2013): 1-6.
12. "Organic material" (n.d.). [Online] Available at:  
[http://web.donga.ac.kr/seojh/Research\\_OrganicMaterials.html](http://web.donga.ac.kr/seojh/Research_OrganicMaterials.html).
13. Clarke, Tracey M., and James R. Durrant. "Charge photogeneration in organic solar cells." *Chemical reviews* 110, no. 11 (2010): 6736-6767.
14. Raymond, Chang, and Overby Jason. *General chemistry-The Essential Concepts*. McGraw-Hill, 2008.
15. Tuček, Jiří, Piotr Błoński, Juri Ugolotti, Akshaya Kumar Swain, Toshiaki Enoki, and Radek Zbořil. "Emerging chemical strategies for imprinting magnetism in

- graphene and related 2D materials for spintronic and biomedical applications." *Chemical Society Reviews* 47, no. 11 (2018): 3899-3990.
16. "Homo-Lumo Interactions - Planning Organic Syntheses: Organic Chemistry." pharmacy180.com. Accessed June 23, 2021. [Online] Available at: <http://www.pharmacy180.com/article/homo-lumo-interactions-1543/>.
17. He, Ming, Feng Qiu, and Zhiqun Lin. "Conjugated rod-coil and rod-rod block copolymers for photovoltaic applications." *Journal of Materials Chemistry* 21, no. 43 (2011): 17039-17048.
18. Wang, Lei, Haiqing Liu, Robert M. Konik, James A. Misewich, and Stanislaus S. Wong. "Carbon nanotube-based heterostructures for solar energy applications." *Chemical Society Reviews* 42, no. 20 (2013): 8134-8156.
19. Savoie, Brett M., Nicholas E. Jackson, Lin X. Chen, Tobin J. Marks, and Mark A. Ratner. "Mesoscopic features of charge generation in organic semiconductors." *Accounts of chemical research* 47, no. 11 (2014): 3385-3394.
20. César Tomé César Tomé is the editor of Mapping Ignorance. "The-Mechanism-of-an-Opv-Device." Mapping Ignorance. Dinahosting, October 13, 2016. [Online] Available at: <https://mappingignorance.org/2016/10/14/organic-photovoltaic-advantages-challenges/figure-1-the-mechanism-of-an-opv-device/>.
21. Alsufyani, Wejdan. "Spectroscopy of Charge-Transfer States in Non-fullerene Acceptor Organic Solar Cells." PhD diss., 2019.
22. Almasabi, Khulud M. "Closing the Lab-to-Fab Gap with Inkjet-Printed Organic Photovoltaics." PhD diss., 2019.

23. Mauer, Ralf. "Charge generation, transport and recombination in organic solar cells." PhD diss., Universitätsbibliothek Mainz, 2012.
24. "Quantum Efficiency." Wikipedia. Wikimedia Foundation, May 17, 2021.  
[Online] Available at: [https://en.wikipedia.org/wiki/Quantum\\_efficiency](https://en.wikipedia.org/wiki/Quantum_efficiency).
25. "Solar Cell Operation." PVEducation. [Online] Available at:  
<https://www.pveducation.org/pvcdrom/graphs>.
26. McDowell, Caitlin, Maged Abdelsamie, Michael F. Toney, and Guillermo C. Bazan. "Solvent additives: key morphology-directing agents for solution-processed organic solar cells." *Advanced Materials* 30, no. 33 (2018): 1707114.
27. Das, Raj, and Avishek Chanda. "Fabrication and Properties of Spin-Coated Polymer Films." In *Nano-size Polymers*, pp. 283-306. Springer, Cham, 2016.
28. <http://www.spincoater.com/what-is-spin-coating.php>
29. Organic Heterojunctions in Solar Cells. [Online] Available at:  
[http://depts.washington.edu/cmditr/modules/opv/organic\\_heterojunctions\\_in\\_solar\\_cells.html#:~:text=The%20electron%20affinity%20can%20be,energy%20of%20the%20LUMO%20level.&text=In%20this%20diagram%20the%20ionization,electron%20affinity%20of%20the%20donor](http://depts.washington.edu/cmditr/modules/opv/organic_heterojunctions_in_solar_cells.html#:~:text=The%20electron%20affinity%20can%20be,energy%20of%20the%20LUMO%20level.&text=In%20this%20diagram%20the%20ionization,electron%20affinity%20of%20the%20donor).
30. Karuthedath, Safakath, Julien Gorenflot, Yuliar Firdaus, Neha Chaturvedi, Catherine SP De Castro, George T. Harrison, Jafar I. Khan et al. "Intrinsic efficiency limits in low-bandgap non-fullerene acceptor organic solar cells." *Nature Materials* 20, no. 3 (2021): 378-384.

31. Yang, Chenyi, Jianqi Zhang, Ningning Liang, Huifeng Yao, Zhixiang Wei, Chang He, Xiaotao Yuan, and Jianhui Hou. "Effects of energy-level offset between a donor and acceptor on the photovoltaic performance of non-fullerene organic solar cells." *Journal of Materials Chemistry A* 7, no. 32 (2019): 18889-18897.
32. Sichula, Vincent A. "Flavins and Their Analogues as Natural and Artificial Catalysts." PhD diss., Bowling Green State University, 2011.
33. Libretexts. "Marcus Theory for Electron Transfer." Chemistry LibreTexts. Libretexts, January 5, 2021. [Online] Available at:  
[https://chem.libretexts.org/Bookshelves/Physical\\_and\\_Theoretical\\_Chemistry\\_Textbook\\_Maps/Time\\_Dependent\\_Quantum\\_Mechanics\\_and\\_Spectroscopy\\_\(Tokmakoff\)/15%3A\\_Energy\\_and\\_Charge\\_Transfer/15.05%3A\\_Marcus\\_Theory\\_for\\_Electron\\_Transfer](https://chem.libretexts.org/Bookshelves/Physical_and_Theoretical_Chemistry_Textbook_Maps/Time_Dependent_Quantum_Mechanics_and_Spectroscopy_(Tokmakoff)/15%3A_Energy_and_Charge_Transfer/15.05%3A_Marcus_Theory_for_Electron_Transfer).
34. Coffey, David C., Bryon W. Larson, Alexander W. Hains, James B. Whitaker, Nikos Kopidakis, Olga V. Boltalina, Steven H. Strauss, and Garry Rumbles. "An optimal driving force for converting excitons into free carriers in excitonic solar cells." *The Journal of Physical Chemistry C* 116, no. 16 (2012): 8916-8923.
35. Khan, Jafar Iqbal, Raja Shahid Ashraf, Maha A. Alamoudi, Mohammed N. Nabi, Hamza N. Mohammed, Andrew Wadsworth, Yuliar Firdaus et al. "P3HT Molecular Weight Determines the Performance of P3HT: O-IDTBR Solar Cells." *Solar RRL* 3, no. 8 (2019): 1900023.
36. Strohm, S., F. Machui, S. Langner, P. Kubis, Nicola Gasparini, Michael Salvador, Iain McCulloch, H-J. Egelhaaf, and C. J. Brabec. "P3HT: non-fullerene acceptor based large area, semi-transparent PV modules with power conversion

- efficiencies of 5%, processed by industrially scalable methods." *Energy & Environmental Science* 11, no. 8 (2018): 2225-2234.
37. "Fullerene." *Encyclopædia Britannica*. Encyclopædia Britannica, inc. [Online] Available at: <https://www.britannica.com/science/fullerene>.
38. He, Youjun, and Yongfang Li. "Fullerene derivative acceptors for high performance polymer solar cells." *Physical chemistry chemical physics* 13, no. 6 (2011): 1970-1983.
39. Hou, Jianhui, Olle Inganäs, Richard H. Friend, and Feng Gao. "Organic solar cells based on non-fullerene acceptors." *Nature materials* 17, no. 2 (2018): 119-128.
40. Wang, Jiayu, and Xiaowei Zhan. "Fused-Ring Electron Acceptors for Photovoltaics and Beyond." *Accounts of Chemical Research* (2020): 1170-1174. Di Carlo Rasi, Dario, and René AJ Janssen. "Advances in solution-processed multijunction organic solar cells." *Advanced Materials* 31, no. 10 (2019): 1806499.
41. Yang, Chenyi, Shaoqing Zhang, Junzhen Ren, Mengyuan Gao, Pengqing Bi, Long Ye, and Jianhui Hou. "Molecular design of a non-fullerene acceptor enables a P3HT-based organic solar cell with 9.46% efficiency." *Energy & Environmental Science* 13, no. 9 (2020): 2864-2869
42. Wang, Jiayu, and Xiaowei Zhan. "Rylene diimide electron acceptors for organic solar cells." *Trends in Chemistry* 1, no. 9 (2019): 869-881.
43. Balawi, Ahmed H., Zhipeng Kan, Julien Gorenflot, Paola Guarracino, Neha Chaturvedi, Alberto Privitera, Shengjian Liu et al. "Quantification of

Photophysical Processes in All-Polymer Bulk Heterojunction Solar Cells." Solar RRL 4, no. 6 (2020): 2000181.

44. Granite, Site by. "Transient Absorption." Edinburgh Instruments, April 15, 2021. [Online] Available at: [https://www.edinst.com/blog/pump-probe-transient-absorption-spectroscopy/#:~:text=Transient%20absorption%20\(TA\)%20spectroscopy%2C,molecules%2C%20materials%2C%20and%20devices.](https://www.edinst.com/blog/pump-probe-transient-absorption-spectroscopy/#:~:text=Transient%20absorption%20(TA)%20spectroscopy%2C,molecules%2C%20materials%2C%20and%20devices.)